


RESEARCH ARTICLE

Structural and molecular characterization of astrocyte and vasculature connectivity in the mouse hippocampus and cortex

Charlotte Lorin¹  | Romain Guet²  | Nicolas Chiaruttini² |
Giovanna Ambrosini^{3,4} | Elvis Boci¹ | Marwan Abdellah¹ | Henry Markram¹ |
Daniel Keller¹

¹Blue Brain Project, Swiss Federal Institute of Technology Lausanne (EPFL), Campus Biotech, Geneva, Switzerland

²Bioimaging and Optics Platform, Swiss Federal Institute of Technology Lausanne (EPFL), Lausanne, Switzerland

³Bioinformatics Competence Center, Swiss Federal Institute of Technology Lausanne (EPFL), Lausanne, Switzerland

⁴Bioinformatics Competence Center, University of Lausanne, Lausanne, Switzerland

Correspondence

Daniel Keller, Blue Brain Project, Swiss Federal Institute of Technology Lausanne (EPFL), Campus Biotech, 1202 Geneva, Switzerland.
Email: daniel.keller@epfl.ch

Funding information

ETH Board of the Swiss Federal Institutes of Technology

Abstract

The relation of astrocytic endfeet to the vasculature plays a key functional role in the neuro-glia-vasculature unit. We characterize the spatial organization of astrocytes and the structural aspects that facilitate their involvement in molecular exchanges. Using double transgenic mice, we performed co-immunostaining, confocal microscopy, and three-dimensional digital segmentation to investigate the biophysical and molecular organization of astrocytes and their intricate endfoot network at the micrometer level in the isocortex and hippocampus. The results showed that hippocampal astrocytes had smaller territories, reduced endfoot dimensions, and fewer contacts with blood vessels compared with those in the isocortex. Additionally, we found that both connexins 43 and 30 have a higher density in the endfoot and the former is overexpressed relative to the latter. However, due to the limitations of the method, further studies are needed to determine the exact localization on the endfoot. The quantitative information obtained in this study will be useful for modeling the interactions of astrocytes with the vasculature.

KEYWORDS

astrocyte, connexin 30, connexin 43, endfeet, hippocampus, isocortex, vasculature

1 | INTRODUCTION

Proper cerebral function relies not only upon neurons but also on protoplasmic astrocytes. These specialized cells play a pivotal role in a variety of physiological pathways, encompassing neurogenesis, synaptic maintenance, and molecular homeostasis (Allen & Lyons, 2018; Eroglu & Barres, 2010; McNeill et al., 2021; Verkhratsky & Nedergaard, 2018). Notably, astrocytes establish physical connections between neurons and cerebral blood vessels (BVs), forming the neuro-glia-vascular (NGV) unit (Aten et al., 2022; Panchenko et al., 2023). They also act as functional gateways, facilitating the coordinated exchange of

ions and metabolites (Abbott et al., 2006; Dunn et al., 2013; Venkat et al., 2017; Zisis et al., 2021).

The intricate spatial organization of astrocytes is based on their star-shaped morphology (Aten et al., 2022; Refaeli et al., 2021; Salmon et al., 2023). Multiple major processes emerge from the astrocyte soma, extend, and progressively ramify into finer branchlets and leaflets (González et al., 2020; Khakh & Sofroniew, 2015; Kim et al., 2019; Lanjakornsiripan et al., 2018; Moye et al., 2019). Astrocytes interact with diverse brain cells, including neurons (Refaeli et al., 2021; Saint-Martin & Goda, 2023), oligodendrocytes (Molina-Gonzalez et al., 2023), other astrocytes (Aten et al., 2022; Kiyoshi & Zhou, 2019), and microglia (Matejuk & Ransohoff, 2020; Pathak &

This is an open access article under the terms of the [Creative Commons Attribution](https://creativecommons.org/licenses/by/4.0/) License, which permits use, distribution and reproduction in any medium, provided the original work is properly cited.

© 2024 The Author(s). GLIA published by Wiley Periodicals LLC.



Sriram, 2023). Furthermore, astrocytic extensions can also contact specialized functional compartments such as synaptic clefts (Aten et al., 2022; Benarroch, 2005; Salmon et al., 2023) and BVs (Hösl, Zuend, et al., 2022; Salmon et al., 2023).

BVs are ensheathed by dedicated and enlarged subcellular astrocytic protrusions called endfeet (Ef) (Bayraktar et al., 2020; Khakh & Sofroniew, 2015; Moye et al., 2019; Vasile et al., 2017). Physically, Ef intricately interdigitate with and almost completely cover cerebral BV networks. Thus, they act as a protective barrier, termed the glia limitans (Owens et al., 2008), that helps support and maintain the integrity of the blood–brain barrier (BBB) by forming its innermost layer (Abbott et al., 2006; Horng et al., 2017; Mathiesen et al., 2010; Moye et al., 2019; Pandit et al., 2020; Quintana, 2017). At the molecular level, Ef are specifically adapted for the two-way exchange of ions and metabolites between the systemic blood circulation and the brain (Cibelli et al., 2021; De Bock et al., 2017; Galea, 2021; Huang et al., 2021; Obermeier et al., 2013). These mechanisms rely on a network of scaffolding, signaling, and cytoskeletal proteins intricately interconnected with channels and transporters.

The aquaporins (AQPs), a family of transmembrane channels with 13 isoforms, allow passive osmotic diffusion of water (Agre, 1997; Clément et al., 2020; Haj-Yasein et al., 2012; MacAulay, 2021). In the central nervous system (CNS), AQP-1 and nine other isoforms are present. AQP-4 is the most abundantly expressed and localized in Ef (Cibelli et al., 2021; Salman et al., 2022). AQP-4 aggregates into orthogonal arrays of particles and anchors the plasma membrane through cytoplasmic interactions with the scaffolding dystrophin-associated protein complex (Haj-Yasein et al., 2011; Lorin et al., 2013; MacAulay, 2021; Nielsen et al., 1997; Tait et al., 2008; Welling, 2008). The resulting supramolecular structures optimize water permeability at the BBB interface (Haj-Yasein et al., 2011; Palazzo et al., 2019), and contribute to the maintenance of Ef ultrastructural integrity (Eilert-Olsen et al., 2012; Neely et al., 2001).

Gap junctions (GJs) also contribute to astrocytic molecular exchange by forming an extensive syncytium that connects astrocytes with brain cells and functional compartments. To accomplish this, six connexins (Cxs), basic protein units, assemble into a structure called a connexon, which can then either function as a hemichannel or contact another connexon located in an adjacent cell membrane to form a GJ (Van Campenhout et al., 2021). Multiple GJs can further aggregate into plaques, which significantly enhance intercellular diffusion of molecules up to 1.5 kDa (Boulay et al., 2018; Bruzzone et al., 1996). In the CNS, depending on the neuroglial cell type and developmental stage (De Bock et al., 2014; John Lin et al., 2017; Nagy et al., 2004; Nakase & Naus, 2004), 11 Cx isoforms have been identified. Notably, Cx43 and Cx30 are predominantly expressed and enriched in astrocytes (Belousov et al., 2017; Boulay, Saubaméa, et al., 2015; Cibelli et al., 2021; Huang et al., 2021; Theofilas et al., 2017). These two Cxs play essential roles in intercellular communication (Sánchez et al., 2020) and endfoot-blood vessel exchanges (Boulay, Saubaméa, et al., 2015; Ezan et al., 2012; Huang et al., 2021; Rouach et al., 2008; Simard et al., 2003).

We have previously developed methods to generate accurate neuroglial models integrated into the intricate organization of the

NGV system (Abdellah et al., 2021; Markram et al., 2015; Zisis et al., 2021). However, despite the intensive use of knockout (KO) mice, some fundamental structural astrocyte-related mechanisms remain elusive and/or controversial (Zhang et al., 2019). For instance, under control conditions, AQP-4, Cx30, and Cx43 KO mice retain preserved BBB and Ef architectures (Fukuda et al., 2013; Ma et al., 1997; Verkhatsky & Nedergaard, 2018), whereas under stress, such as high vascular hydrostatic pressure, the BBB appears either intact (Eilert-Olsen et al., 2012; Fukuda et al., 2013; Kubotera et al., 2019; Saadoun et al., 2009) or, conversely, abnormally permeable, together with astrocytic Ef swelling (Bordoni et al., 2023; Cibelli et al., 2021; Ezan et al., 2012; Zhou et al., 2008). Collectively, these observations primarily confirm that Cxs and AQPs can equally contribute structurally to the BBB and Ef, beyond their molecule exchange functions. Nevertheless, they concurrently highlight the sparseness of knowledge about the detailed cytoarchitectures linking AQP-4, Cxs, Ef, and BVs.

To address these architectural gaps, our study investigated the biophysical and molecular organization of astrocytes and their intricate Ef network at the micrometer level within the isocortex (IsoCx) (Salmon et al., 2023) and hippocampus (Hipp) (Refaeli et al., 2021). These two distinct yet interconnected brain regions are of particular interest due to their central role in cognitive task performance and memory consolidation (Lawal et al., 2022; Wang et al., 2022), making them prime targets for neuropathologies, including Alzheimer's disease (Endo et al., 2022; Planche et al., 2022), amyotrophic lateral sclerosis (Zhou et al., 2016), and major depressive disorder (Zhang et al., 2018).

In our investigation, we used double transgenic mice to perform co-immunostaining, confocal microscopy, and three-dimensional (3D) digital segmentation. Our results reveal that hippocampal astrocytes exhibited significantly smaller territories along with reduced Ef dimensions and Ef-BV contact surfaces. Remarkably, most astrocytes established contact with three BVs, with potential interactions reaching up to seven in IsoCx. In contrast, within Hipp, these numbers decrease to two and six vessels, respectively. Collectively, these intriguing data suggest that regionally specialized gliovascular networks cater to the specific requirements of distinct brain areas, certainly driven by tailored underlying molecular mechanisms (Endo et al., 2022). Considering their pivotal role in the compound exchange, Cxs may be part of this versatile plasticity. Therefore, we conducted extensive analyses of the Cx43 and Cx30 clusters and density distributions. Despite similar protein abundances observed in both IsoCx and Hipp, a substantial expression disparity between these two Cxs emerged within subastrocytic compartments and BVs. Specifically, overexpression of Cx43 relative to Cx30 was detected, especially in Ef compartments, where protein clusters appeared predominantly localized in the cytoplasm, suggesting readily mobilized reserve pools of Cxs.

2 | MATERIALS AND METHODS

Experimentally, data were generated from genetically modified mice involved in multiple assays as described below.

2.1 | Animals

For the expression of tdTomato fluorescent proteins in astrocytes, the Ai14 mouse line (Rosa-CAG-LSL-tdTomato, stock #007914, Jackson Laboratory, United States) (Madisen et al., 2010) was bred with human glial fibrillary acidic protein (hGFAP)-CreERT2 (a Cre recombinase [Cre] fused to a mutant estrogen ligand binding domain [ERT2]) mouse lines (Stock #012849, Jackson Laboratory, United States) (Ganat et al., 2006) to generate hGFAP-CreERT2/+;Rosa26-floxed-STOP-tdTomato transgenic mice, used as a tamoxifen (TAM)-inducible mouse model (Figures S1 and S2).

Through a yet uncharacterized molecular mechanism, the sex of the mouse parents interfered with the expression of tdTomato in astrocytes following TAM injections as shown in Figure S2B. Therefore, only LSL-tdTomato females were crossbred with CreERT2 males to generate individuals with the expected inducible tdTomato expression (Figures S1 and S2A). During the breeding, animals were mated in suitable cages and maintained on a 12-h light-dark cycle with free access to food and water.

All animal experiments described in this paper were performed in accordance with the Swiss Welfare Act and the Swiss National Institutional and Veterinary office guidelines in the Canton of Vaud on Animal Experimentation for the ethical use of animals.

2.2 | Genotyping

Mouse toe clipping was performed to identify the hGFAP-CreERT2/+;Rosa26-floxed-STOP-tdTomato transgenic mice, bred in the animal facility. Biopsies of phalanges, a maximum of one phalanx per paw and a maximum of two per animal were collected between postnatal days 5 (P5) and P12 for subsequent use in a standard genotyping protocol by polymerase chain reaction (PCR) (Figure S1B).

Samples were digested for 4 h at 56°C under shaking at 900 rounds per minute (rpm), using 0.2 mg/mL of proteinase K (3115887001, Merck) in the DirectPCR Lysis reagent (VIG102-T, Viagen Biotech). After the inactivation of the enzyme by a 45-min incubation at 84°C under agitation at 700 rpm, the supernatant containing deoxyribonucleic acid (DNA) was used for genotyping. A first master mix was prepared for the Rosa-CAG-LSL-tdTomato mouse lines and contained Kapa 2G Fast Multiplex Mix (KK5802, Merk), 0.2 μM IMR 9020 long (5'-GT AAG GGA GCT GCA GTG GAG TA GGC-3'), 0.2 μM IMR 9021 long (5'-CCG AAA ATC TGT GGG AAG TC TTG TCC-3'), 0.2 μM IMR 9103 short (5'-C ATT AAA GCA GCG TAT CC-3'), 0.2 μM IMR 9105 short (5'-CTG TTC CTG TAC GGC ATG-3'), bromophenol blue 1%, and double distilled water (ddH₂O). A second master mix was prepared for the hGFAP-CreERT2 mouse lines and contained Kapa 2G Fast Multiplex Mix (KK5802, Merk), 0.2 μM primer 10898 (5'-GCC AGT CTA GCC CAC TCC TT-3'), 0.2 μM primer 10899 (5'-TCC CTG AAC ATG TCC ATC AG-3'), 0.2 μM IMR 7338 (5'-CTA GGC CAC AGA ATT GAA AGA TCT-3'), 0.2 μM IMR 7339 (5'-GTA GGT GGA AAT TCT AGC ATC ATC C-3'), and ddH₂O. PCR mixes consisted of 10 μL of master mix and 2 μL DNA sample. PCR reactions were

performed on the Sensoquest system using the following cycle: (1) 95°C, 3 min; (2) 95°C, 15 s; (3) 60°C, 30 s; (4) 72°C, 30 s; steps 2–4 were repeated 30 times; and (5) 10°C. Finally, the reaction products were run on a 2% agarose gel (11405.01, Serva) in TBE 1X (89 mM Tris, A 1086.5000, Applichem; 89 mM boric acid, A 2940.1000, Applichem; 2 mM ethylenediamine tetraacetic acid [EDTA], A 1103.0500, Applichem) at 75 V.

2.3 | Tamoxifen injection

To induce the genetic deletion of STOP codons in hGFAP-CreERT2/+;Rosa26-floxed-STOP-tdTomato transgenic mice and to trigger the expression of hGFAP-tdTomato fluorescent proteins in sparse astrocytes, 7-week-old individuals (between P43–47) received an intraperitoneal (i.p.) injection of TAM solution daily for five consecutive days at a dose of 75 mg/kg body weight (T5648, Merk) (Figure S1C) (Hösl, Binini, et al., 2022; Park et al., 2018; Schreiner et al., 2015; Srinivasan et al., 2016). TAM solution (20 mg/mL emulsion dissolved overnight at 37°C in sunflower seed oil, 88921, Merk) was always aliquoted and frozen at –20°C until use. As displayed in Figure S1C, 7 days after TAM treatment, 8-week-old (P54–58) mice were euthanized, brains were extracted and cut into 300 or 150 μm thick parasagittal slices, depending on the type of subsequent experiments, electrophysiology (Figure S3), or immunostaining (Figure 1a).

2.4 | Parasagittal brain slice preparation

HGFAP-CreERT2/+;Rosa26-floxed-STOP-tdTomato transgenic mice between P54–58 were rapidly anesthetized with isoflurane (5% in oxygen) in a gas chamber and decapitated. Brains were removed and placed in iced artificial cerebrospinal fluid (ACSF) containing (in millimolar (mM)): 125 NaCl, 25 NaHCO₃, 2.5 KCl, 1.25 NaH₂PO₄, 2 CaCl₂, 1 MgCl₂, and 25 D-glucose. Slices of either 300 μm-thickness for patch clamp experiments (Figure S3) or 150 μm thickness for histology and immunostainings, were then carefully cut in the parasagittal plane at 4°C with a vibratome to maintain consistent orientation of brain areas, BVs, cells, and Ef. It was important to ensure consistent orientation in order to accurately compare results from different slices (Leica VT1200S, Leica) (Figure 1a).

2.5 | Electrophysiology

After brain slicing, 300-μm-thick parasagittal slices were placed in ACSF, bubbled with 95% O₂-5% CO₂, and allowed to recover for at least 1 h at room temperature (RT) before whole-cell patch-clamp recording (Figure S3). A brain slice was then transferred to the recording chamber mounted on an upright microscope (Luigs & Neumann, Ratigen, Germany) with constant perfusion of oxygenated ACSF. Using a VX44 infrared differential interference contrast video camera (PCO CCD Imaging, Kelheim, Germany) and a QuantEM™ 512SC

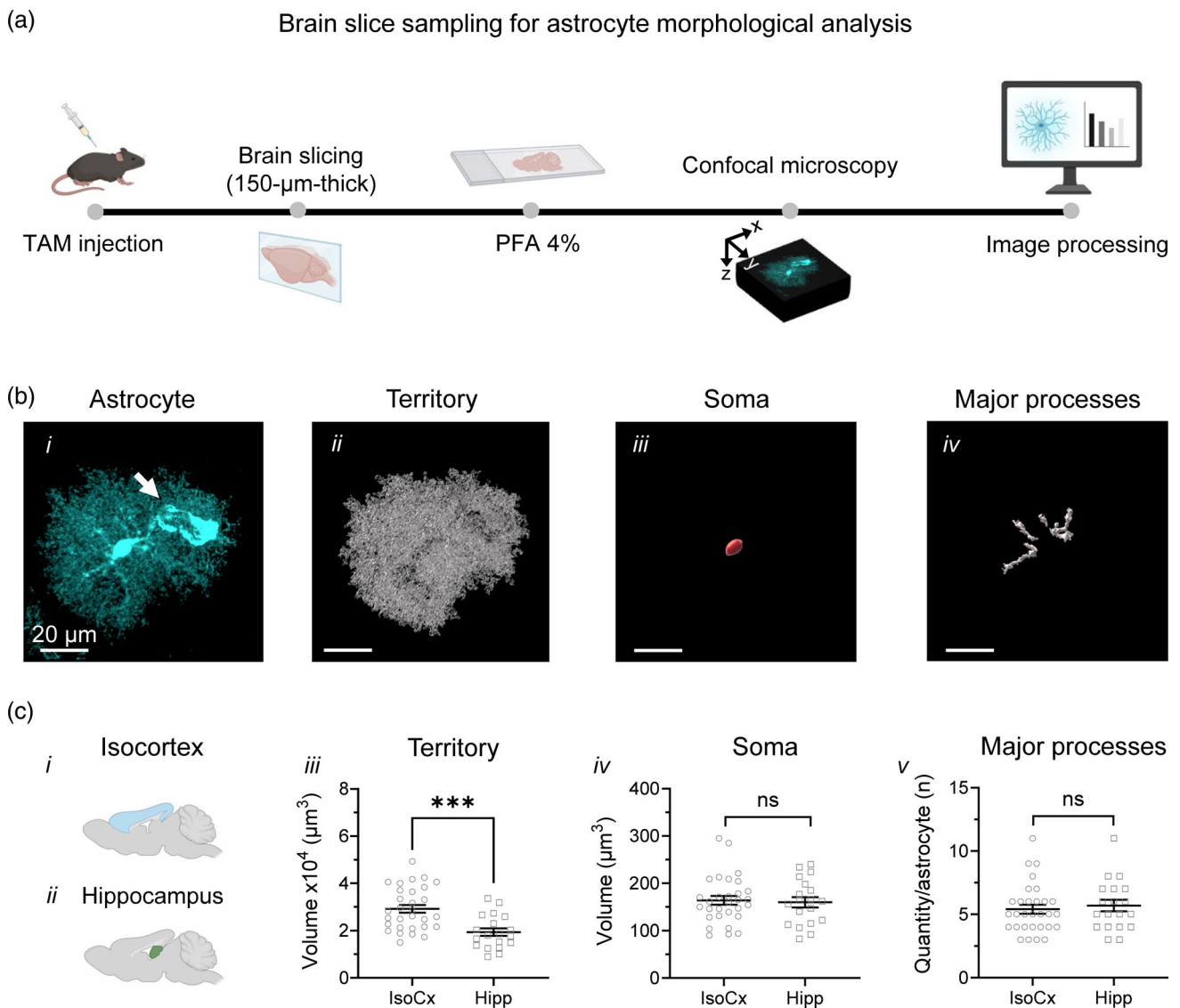


FIGURE 1 Morphological analysis of cortical and hippocampal astrocytes. (a) Stepwise process illustrating the workflow, from sampling 150- μm -thick brain slices of 8-week-old double transgenic mice (previously injected with tamoxifen according to the protocol described in Figure S1 and Materials and Methods) to 3D image acquisition and processing by confocal microscopy (Figure S8). (b) Representative tdTomato fluorescent cortical astrocyte (i) with an endfeet (white arrow). 3D digital reconstructions in 0° orientation of the cell territory (ii), soma (iii), and major processes (iv). Scale bar = 20 μm . (c) Schematic parasagittal brain slices depicting the IsoCx (blue, i) and Hipp (green, ii), respectively. Analysis of AT ($\times 10^4$, μm^3 , iii) and soma (μm^3 , iv) volumes, as well as the quantity of major processes per astrocyte (n, v) in IsoCx (white circles) and Hipp (white squares). $n = 30$ astrocytes, $N = 7$ mice for IsoCx; $n = 19$ astrocytes, $N = 5$ mice for Hipp. Data are presented as Mean \pm SEM; *** $p < .001$, not significant (ns) $p > .05$, statistically tested by linear mixed models fit by restricted maximum likelihood (Table S6). The cartoons were created with BioRender.com.

fluorescence camera (Photometrics, Tucson, AR) with an LED illumination system pT-100 (CoolLED, Andover, NY), astrocytes in IsoCx were localized and identified based on soma morphology and size as well as tdTomato fluorescence (Figure 3b). Subsequently, whole-cell recordings were performed (Figure S3C) using a MultiClamp 700B amplifier (Molecular Devices, Union City, CA, USA), Igor Pro 7.08 software (WaveMetrics, Portland, OR, USA), and borosilicate glass pipettes (9–12 M Ω , #1403513, Hilgenberg GmbH, Malsfeld, Germany) pulled from a Flaming/Brown micropipette puller (DMZ Universal Puller; Zeitz-Instrumente, Munich, Germany) and

containing (in mM): 110 K-gluconate, 10 KCl, 4 Mg-ATP, 10 Na-phosphocreatine, 0.3 Na-GTP, 10 HEPES, pH 7.2 (adjusted with 5 M KOH), and 300 mOsm (adjusted with D-mannitol 25–35 mM). We measured membrane capacitance (C_m) and resting membrane potential (E_m) (Figure S3D-ii). Finally, we applied a voltage clamp protocol in which the voltage was stepped from -90 to 20 mV in 10 mV increments (Figure S3C-i). The membrane current was recorded to generate I/V (current/voltage) curves (Figure S3D-i), from which the input resistance (slope, R_{input}) was extracted (Figure S3D-ii) (Ma et al., 2014; Zhou et al., 2021).

2.6 | Histology and immunohistochemistry

After brain slicing, 150 μm thick parasagittal sections were fixed in 4% paraformaldehyde (PFA) (prepared in 0.1 M phosphate buffer, pH 7.4) for 15 min, followed by three washes of 5 min each with 0.1 M phosphate buffer solution (PBS) (Figure 1a). Then, brain slices were either stored at 4°C in 0.1 M PBS until use for immunostaining or mounted in fluorescence mounting medium (S3023, Dako) on Superfrost™ Plus adhesion slides (J1800AMNZ, Thermo Scientific), dried overnight and stored in the refrigerator until microscopy acquisition and histological analysis.

For immunostaining, 4% PFA-fixed brain slices were washed three times in 0.1 M PBS with 0.5% Triton X-100 (A4975, AppliChem) for 5 min each. The slices were incubated for 1 h at RT, with gentle shaking in a blocking solution containing 0.1 M PBS, 0.5%, Triton X-100, and 10% normal goat serum (NGS, S-1000-20, Vector Laboratories). Brain sections were then placed at RT with gentle agitation in a solution containing 0.1 M PBS, 0.5% Triton X-100, and 5% NGS including the following primary antibodies: rabbit polyclonal anti-AQP-4 (1:80, NBP1-87679, Novus Biologicals), mouse monoclonal anti-Cx43 conjugated to Alexa Fluor™ 488 (1:20, 138388, ThermoFisher Scientific), mouse monoclonal anti-Cx30 (1:20, MA5-35021, ThermoFisher Scientific), or rabbit polyclonal anti-aldehyde dehydrogenase 1 family member L1 (ALDH1L1, ab87117, Abcam) for 3 days. Then, the samples were washed three times in a solution of 0.1 M PBS, 0.5%, Triton X-100, and 10% NGS for 10 min each and incubated for 6 h at RT with secondary antibodies: alpaca anti-rabbit IgG DyLight™ 405 conjugated (1:3000, 611-474-215, Jackson ImmunoResearch Laboratories), alpaca anti-mouse IgG2b Alexa Fluor™ 488 conjugated (1:3000, SMS2BAF488-1-10, Lubo Science), or alpaca anti-human IgG/anti-rabbit IgG Alexa Fluor™ 488 conjugated (1:3000, SRBAF488-1-10, Lubo Science). Next, the samples were rinsed three times with a solution of 0.1 M PBS supplemented with 0.5%, Triton X-100, and 5% NGS for 10 min each, followed by incubation at RT, overnight, with isolectin GS-IB₄ from *Griffonia simplicifolia* (IB₄) conjugated to Alexa Fluor™ 647 (1:3000, I32450, ThermoFisher Scientific). To complete the immunostaining, three washes with 0.1 M PBS solution were performed before incubation for 20 min in a solution of 0.1 M PBS containing 4',6-diamidino-2-phénylindole (DAPI, 1:50000, D9542, Sigma). Finally, the sections were washed three times for 10 min each in 0.1 M PBS before mounting in fluorescence mounting medium (S3023, Dako) on Superfrost™ Plus adhesion slides (J1800AMNZ, Thermo Scientific), dried overnight, and stored in the fridge until microscopy acquisition and analysis. Negative controls were also performed by adding secondary antibodies only to the brain slices (data not shown).

2.7 | Confocal microscopy

Confocal microscopy was performed using an upright confocal microscope (Upright Leica SP8 DM6 CS), equipped with a 40 \times (1.25

numerical aperture [NA], HC PL APO CS2) glycerol immersion objective (Leica). To test for the most suitable objective, initial imaging experiments were performed with both 40 \times glycerol and 63 \times oil (1.4 NA) objectives on the exact same cell sample with an identical voxel size of 86 nm (xy) and 180 nm (z) (Figure S4 and Table S1). Cross sections of these two z stacks were generated by rotating the stacks at 90° around the x-axis and then projected using maximum intensity projection (Figure S4A). For each objective, the signal intensity of each fluorescence (tdTomato, Cx43, AQP-4, and IB₄) was plotted as a function of depth (z) (Figure S4B). Since the 40 \times glycerol objective minimizes aberrations caused by the refractive index mismatch between immersion medium and the biological sample, it significantly reduces fluorescence loss along the z-axis. Therefore, subsequent experiments were conducted using this objective.

To ensure complete imaging of the cell, the z dimensions of the images were adjusted based on the fluorescence signal emitted by the tdTomato-labeled astrocytes. Considering that astrocytic processes can be as thin as 50–100 nm in diameter, falling below the diffraction limit of conventional light microscopy (200–300 nm) (Heller & Rusakov, 2019), z-axis acquisition was initiated and ended when tdTomato fluorescence was no longer visually detectable. The depth of z-axis acquisition varied depending on the volume of the astrocyte.

For both IsoCx and Hipp, we assessed the variation in fluorescence intensity for each antibody (AQP-4, IB₄, Cx43, and Cx30) across 40- μm thick brain slices (Figures S5 and S6). To achieve this, cross-sections of all astrocyte images used in our study were generated by rotating the z-stacks by 90° around the y-axis and then projected using maximum intensity projection (Figures S5A-ii, S5B-ii, S5B-iii, S5C-ii, S5D-ii, S6A-ii, S6B-ii, S6B-iii, S6C-ii, and S6D-ii). The resulting fluorescence intensity profile for each antibody was normalized by subtracting the autofluorescence measured on a control sample and dividing by the maximum measured intensity over the z-axis (Figures S5A-i, S5B-i, S5C-i, S5D-i, S6A-i, S6B-i, S6C-i, and S6D-i, and Table S1). At the deepest point in the brain slices (40- μm thick), 29% and 37% of the AQP-4 signal remained (Figures S5C-i and S6C-i), 69% and 82% for IB₄ (Figures S5D-i and S6D-i), 24% and 65% for Cx43 (Figures S5B-i and S6B-i, yellow); and 19% and 35% for Cx30 (Figures S5B-i and S6B-i, magenta), in IsoCx and Hipp, respectively. Achieving equal antibody accessibility to epitopes throughout the tissue thickness is critical to staining homogeneity, a prerequisite for accurate quantitative analysis and comparisons (Yau et al., 2023; Zwang et al., 2023). However, as shown in Figures S5 and S6, the penetration depth of antibodies is limited by two main factors. First, the tissue thickness acts as a physical barrier that prevents facilitated diffusion. Second, the nonuniform expression of the target proteins throughout the samples results in the absence of epitopes in some areas, leading to undetectable signals. For instance, tdTomato fluorescence is reduced at the edge of the cell territory, where only fine processes are present, compared to the nearly saturated signal in the soma at the mid-position (Figures S5A-ii and S6A-ii). Consequently, the resulting fluorescence intensity profile is bell-shaped (Figures S5A-i and S6A-i). In our study, for the



anatomical study of astrocytes, the entire cell volume was detected in 3D using tdTomato signals, and those for AQP-4 and IB₄ were necessary to reconstruct Ef and BVs. For molecular characterization, the localization and quantification of Cx43 and Cx30 were of great interest and performed with their respective antibody fluorescence. Since the decays of fluorescence, as previously described for each antibody, did not prevent Imaris software from detecting signals of interest (see Image processing section), and through multiple analyses of negative controls and sample images, we confirmed that the fluorescence intensities over the thickness of interest were sufficient for quantitative analyses and comparisons.

To maximize signal acquisition of AQP-4, Cx43, Cx30, tdTomato astrocytes, and IB₄ staining in the z-plane, a step size of 0.18 μm was used for the stacks. In the xy-plane, the image dimension was fixed at 1352 × 1352, with a zoom factor of 1.2, resulting in a pixel size of 86 nm. For the control experiments performed with DAPI, AQP-4, ALDH1L1, and IB₄ antibodies combined with tdTomato fluorescence, the z-step size was 1 μm between the stacks, the image dimension was fixed at 1024 × 1024, and the zoom factor was 2.5, resulting in a pixel size of 113 nm (Figure S7).

For fluorescence excitation, DyLight™ 405, Alexa Fluor™ 488, tdTomato, and Alexa Fluor™ 647, conjugated to their respective antibodies were excited to 405, 488, 552, and 638 nm, respectively. The laser speed was set to 1000 Hz with a 2-line average per channel. The emitted fluorescences were sequentially detected by two HyD spectral detectors tuned to the 410–480 nm, 500–550 nm, 560–620 nm, and 650–710 nm wavelengths, respectively, and switched between frames. The acquired images were visualized using Leica Application Suite X software (Leica). The 5× (0.15 NA, HC PL FLUO-TAR) dry objective (Leica) and the “tile scan” option of LAS X navigator were used to acquire larger overviews of whole parasagittal brain slices.

2.8 | Deconvolution

To enhance the resolution of the confocal images in the x-y-z dimensions and to improve the signal quality by reducing the noise, deconvolutions were performed using the SVI Huygens software via the Huygens Remote Manager (HRM) (Scientific Volume Imaging B.V., Hilversum, The Netherlands) with the “classic maximum likelihood estimation” algorithm (Ponti et al., 2007).

Before deconvolution, the average background for each channel (AQP-4, Cx43, Cx30, DAPI, ALDH1L1, tdTomato, and IB₄) in each image was measured in Fiji-ImageJ. Briefly, the raw image was split into individual image stacks corresponding to each channel. Then, an area without the signal of interest was manually selected using the rectangle tool in Fiji-ImageJ to measure the background along the z-axis. Only a few z-stacks were selected for DAPI, Cx43, and Cx30, which exhibited staining patterns appearing anywhere in the image. The total background value was then calculated by averaging the obtained measurements. Subsequently, the raw images were imported

into the HRM. A theoretical point spread function (PSF) was selected and the type of microscope and objectives were defined based on the above specifications. A refractive index of 1.37 was specified for the fluorescence mounting medium (S3023, Dako), and the voxel size was defined as an xy pixel size of 86 nm and a z step size of 180 nm. For each co-immunostaining, a deconvolution template was applied, including the previously measured background values, a fixed number of iterations, and the signal-to-noise ratio (SNR). The SNR, defined as the square root of the number of photons in the brightest part of the raw image, was initially calculated by HRM and further refined by the experimenter until the roughness or granularity of the image was restored. Specifically, for datasets combining fluorescence images of tdTomato, Cx43, AQP-4, and IB₄, SNR values of 6, 3, 2, and 3, respectively, were applied to each channel with 30 iterations and a quality change set to 0. For images consisting of tdTomato, Cx30, AQP-4, and IB₄, SNR values of 6, 2, 2, and 6, respectively, were applied with 16 iterations and a quality change set to 0. For images consisting of tdTomato, DAPI, AQP-4, and IB₄, SNR values of 2, 2, 1, and 3, respectively, were applied with 20 iterations and a quality change set to 0. For images consisting of tdTomato, DAPI, ALDH1L1, and IB₄, SNR values of 2, 2, 1, and 3, respectively, were applied with 20 iterations and a quality change also set to 0.

2.9 | Image processing

Processing of the aforementioned deconvolved images was performed using Fiji-ImageJ (Schindelin et al., 2012), Matlab (R2020b, MCR v9.9), and Imaris (BitPlane, South Windsor, CT, USA) (<https://github.com/BIOP/EasyXT-FIJI>) software with a sequence of manual operations and custom Fiji-ImageJ Groovy scripts (10.5281/zenodo.8155041) (Ollion et al., 2013). As displayed in Figure S8, the entire workflow started with the generation of 3D surface models in Imaris. For astrocyte components, such as astrocyte territory (AT), soma, and major processes, the objects were reconstructed based on tdTomato fluorescence (C1, cyan). However, it should be noted that the Imaris software could not discriminate the free spaces between the multiple interlaced fine processes of the astrocytes, which led to the analysis of the AT rather than the strict cell volume. Additionally, if the image was “contaminated” by other astrocytes around the cell of interest, a second filter in the segmentation process, called “distance to image border XY img=1” was added and set to exclude them from the analysis.

The Ef and BV Imaris reconstruction surfaces were built based on AQP-4 and IB₄ staining, respectively (C3, green and C4, red). Throughout the image processing, the parameters remained constant for each element, except for the “Threshold” values and some filters, which were individually adjusted by a trained experimenter to fit each component as finely as possible (Table S2). To validate the variable parameters in Imaris, a binary mask was created, and a visual inspection was performed in Imaris slice mode to ensure that the segmentation matched the signal observed by the trained experimenter. After verification, AT, soma, and BV volume and proportion were obtained from

the statistical option in Imaris, while the number of major processes was manually counted after visual review (Tables S3 and S4).

For further analysis of the BVs, the number of BVs contacted per Ef and astrocyte, as well as their frequency distribution and their diameter were manually determined using the measuring tool in Imaris slice mode (Figure 3 and Table S5). Since the BV network is ultimately just a connected structure, it is important to note that in this study, each subdivision of a main BV was considered as a separate BV.

To prepare the datasets for the next steps of processing and analysis, each image was upsampled using Matlab (Figure S8), which computed the appropriate value in Imaris to generate an isotropic voxel spacing of 86 nm in the z-axis (Table S3). Subsequently, the AT and AQP-4 Imaris surfaces were converted into masks by the Fiji-ImageJ software using the costumed AstroAnalyzer_endFeetFinder_withClusters groovy script (see the 5-Groovy scripts.zip file on Zenodo). The goal of this process was to create a new Ef object surface in Imaris, encompassing all Ef from a single astrocyte, as well as an Ef cluster channel, allowing manual splitting of each Ef into new Imaris surfaces (Ef n). The Ef cluster channel was created by dilating the Ef mask using a spherical structuring element with a radius of 2.5, followed by a 3D connected components analysis (Legland et al., 2016). The resulting label image with clustering information was included as a channel in the Imaris dataset. The AstroAnalyzer_endFeetFinder_withClusters groovy script also generated a compatible Excel file to extract in a table the volume (μm^3) of each Ef according to the “Intensity Median” Ef cluster parameter as a filter field (see Imaris_final_CL230331_E2_serie1_results.csv and Imaris_final_CL230331_E2_serie1_Endfeetanalysis.xlsx on [10.5281/zenodo.8155041](https://doi.org/10.5281/zenodo.8155041) in the 4-Image analysis_CL230331_E2_serie1.zip file). Ef exclusion criteria were applied to retain only the Ef of interest, such as volumes less than $1 \mu\text{m}^3$ and Ef that did not ensheath BVs, visually checked on the 3D image in Imaris by a trained experimenter.

Using the Matlab script “Surface-Surface contact area” in Imaris (<https://imaris.oxinst.com/open/view/surface-surface-contact-area>), an Ef-BV contact surface Imaris object was calculated and created between the BV and Ef Imaris surfaces. Similarly, an AQP-4-AT contact surface (AQP-4-AT cs) Imaris object reflecting the Ef area surfaces was generated between AQP-4 and AT Imaris surfaces using the same Matlab script. Individual Ef-BV and AQP-4-AT Imaris contact surfaces were also created using the Ef cluster channel as a filter parameter. To extract the surface area data (μm^2) and the corresponding proportions into a table, the Get_Surfaces_Stats groovy script in Fiji-ImageJ was used to generate compatible Excel files (See Imaris_final_CL230331_E2_serie1_Endfeet analysis.xlsx, Surfaces Statistics-Contact surface ef-bv_Imaris_final_CL230331_E2_serie1.csv, and Surfaces Statistics-Endfeetsurface_Imaris_final_CL230331_E2_serie1.csv in the 4-Image analysis_CL230331_E2_serie1.zip file on Zenodo, and Tables S3 and S4).

For visualization purposes, segmented volumes from Fiji-ImageJ were converted into optimized and watertight mesh models using Ultralizer (Abdellah et al., 2023). Ultralizer uses solid voxelization to fill the interior volume of the mask and then converts the mask into a

proxy mesh model using the marching cubes algorithm. The surface of this proxy mesh was smoothed using Laplacian smoothing and then optimized to create a watertight manifold based on the algorithm proposed by Attene (Attene, 2010).

For the analysis of Cx43 or Cx30 proteins, Imaris was used to generate 3D spots by modeling Cx clusters based on their corresponding staining (C2, gray, Figure S8). To optimize cluster detection by the software, no filter was applied to the Cx signals to maximize their fluorescence intensity (Table S2). This method compensated for the gradients of Cx signals observed across the tissue thickness, and negative control images were tested to validate it. Following up-sampling, each Imaris surface of interest, including BVs, Soma, AT, Ef, AQP-4-AT, and Ef-BV, was converted into individual Imaris channels. These channels were then combined with the 3D Cx spots using the Get_Spots_Stats groovy script (See the 5-Groovy scripts.zip file on Zenodo) within Fiji-ImageJ to generate a compatible Excel file (Spots Statistics-Imaris_final_CL230331_E2_serie1.csv in the 4-Image analysis_CL230331_E2_serie1.zip file on Zenodo). From the resulting dataset, the number of Cx clusters was extracted in a table depending on the Imaris surface type, that is, AT, soma, BV, Ef, Ef-BV, and AQP-4-AT (Imaris_final_CL230331_E2_serie1_Cx43 analysis.xlsx in the 4-Image analysis_CL230331_E2_serie1.zip file on Zenodo). The obtained values were filtered with the “Intensity Max” channel from each element of interest to subsequently calculate Cx volume and surface densities (Figures 4 and 5, and Table S3). The distribution of Cxs in the Ef cytoplasm was calculated by subtracting Cxs in the AT from those at the Ef surface (Table S3).

To illustrate the entire image processing and analysis workflow, a 3D animation video was produced using the camera option of Imaris (Video S1). The video was edited using Clipchamp software (Microsoft) and depicts the complete reconstructions of an astrocyte, its Ef in contact with BVs, and its Cx43 expression and distribution.

2.10 | Statistical analysis

Statistical analyses and data plots were conducted using GraphPad Prism and R software. Detailed descriptions of the statistical tests used, sample sizes (n for astrocytes and N for animals), and results are available in Table S6 and the figure legends. It is important to note that some of the samples were not independent; specifically, five from both the Hipp and IsoCx were obtained from the same animals. As the data were pooled, resulting in a comparison of 30 isocortical astrocytes from 7 mice and 19 hippocampal cells from five animals, a mixed model statistical approach was applied where appropriate. Data are presented in scatter dot plots and histograms as Mean \pm SEM. Statistical significance was defined as follows: not significant (ns) $p > .05$; $*p < .05$; $**p < .01$; and $***p < .001$.

3 | RESULTS

To generate fluorescent astrocytes in the mouse IsoCx and Hipp, two parental mouse lines, one hemizygous for the hGFAP-CreERT2

transgene and the other homozygous for the LSL-tdTomato allele, were bred as shown in Figures S2A-i and S2B-i. PCRs of the resulting double transgenic litters were performed to confirm the presence of the targeted transgenes (Figures S1A, S2A-ii, and S2B-ii). Figure S1B-i shows the PCR results of three double-mutant mice carrying the hGFAP-CreERT2 transgene, indicated by a band at 200 bp, and the internal positive control, seen as a band at 324 bp. Furthermore, the same individuals were heterozygous for the LSL-tdTomato mutant gene with a band at 196 bp, and the wild-type counterpart band at 297 bp. These validated double-mutant mice were then used as a TAM-inducible model to sparsely induce fluorescence in astrocytes (Figure S1C).

A TAM solution at 75 mg/kg body weight was administered intraperitoneally daily to 7-week-old double transgenic mice for five consecutive days. These injections elicited the nuclear translocation of the CRE enzyme, which was specifically expressed in cells carrying the CreERT2 transgene under the control of the hGFAP promoter (Kim et al., 2018). The translocated Cre recombinase recognized the two repeated lox sites on the DNA and excised the lox-flanked STOP codon (Figure S1C, dotted box), leading to the cellular expression of fluorescent tdTomato proteins (Kim et al., 2018). One week later, at 8-week-old, brains were extracted and sectioned in a parasagittal plane to obtain slices containing fluorescent cells (Figure S1C, maximum intensity projection image). However, due to a still elusive underlying molecular mechanism (Figure S2B-iii), it is worth noting that the parental sex impacted the litter's ability to produce fluorescent cells after TAM injections (Figure S2, <https://www.jax.org/news-and-insights/jax-blog/2013/september/a-dozen-facts-you-didnt-know-about-cre-lox>). Indeed, breeding CreERT2 females to LSL-tdTomato males (Figure S2B-i) resulted in double transgenic mice (Figure S2B-ii) with the expected genotype (Figure S1B), but they were unable to express fluorescent tdTomato proteins in brain cells following TAM injections (Figure S2B-iv). Based on these observations and following the principles of the 3Rs (replace, reduce, refine) (Vitale & Ricceri, 2022), which aim to avoid or reduce animal testing and suffering, the breeding plan for the animal experimentation in this study was refined by crossing only CreERT2 males and LSL-tdTomato females (Figure S2A). The implementation of this strategy minimized the number of experimental animals used and reduced potential distress or discomfort to the animals involved in the study.

After induction of sparse fluorescent cells in the brains of double transgenic mice, cell identity was validated by electrophysiology (Figure S3). After sectioning of parasagittal brain slices at 300- μ m thickness (Figure S3A), cells were selected in the IsoCx area (Figure S3B-i) under a microscope according to several criteria. Cells with uniform fluorescence, well-delineated bushy territories, and an oval soma 10 μ m in diameter, were retained (Figures S3B-ii and S3B-iii). Whole-cell patch clamp recordings were then performed according to the protocol depicted in Figure S3C-i. Specifically, voltage clamp steps were applied from -90 to 20 mV in 10 mV increments, generating membrane current responses, representative traces of which are shown in Figure S3C-ii. Current-voltage relationships were measured from seven cortical cells to generate an average linear I/V curve

typical of nonexcitable cells (Figure S3D-i). The cells exhibited a hyperpolarized resting potential (E_m) of -80.4 ± 0.8 mV, a low input resistance (R_{input}) of 37.6 ± 4.6 mV, and a small capacitance (C_m) of 16.1 ± 4.7 pF (Mean \pm SEM, Figures S3D-ii) compared to neurons (Zhou et al., 2006). Through analysis of the experimental electrophysiological data and the colocalization of tdTomato fluorescence with the ALDH1L1 staining (Figure S7B), these sparse isocortical fluorescent cells exhibited characteristics consistent with literature descriptions of protoplasmic astrocytes (Bolton et al., 2006; Dallérac et al., 2013; Du et al., 2015; McNeill et al., 2021).

Once the fluorescent cells were identified as astrocytes, their morphological hallmarks were analyzed (Figure 1). We focused on two distinct but interconnected brain regions, the IsoCx and the Hipp (Figure 1c-i,c-ii).

Analyses were performed using 3D confocal images of astrocytes following the stepwise workflow described in Figure 1a, S8 and Video S1.

A representative example of the results obtained is shown in Figure 1b. In Figure 1b-i, thanks to tdTomato fluorescence, the astrocyte displayed a typical intricate bushy structure consisting of thin and intertwined branches originating from major processes extending directly from the soma (Moye et al., 2019; Zhou et al., 2019; Zisis et al., 2021). Notably, an enlarged protrusion was observed at the terminal end of one branch (white arrow, Figure 1b-i). This structure, similar to others observed in previous studies (Kubotera et al., 2019), did not colocalize with DAPI staining (Figure S7A), but it did with AQP-4 (Figure 2). Consequently, this protrusion was identified as an Ef.

Next, the astrocyte's components, territory (Figure 1b-ii), soma (Figure 1b-iii), and major processes (Figure 1b-iv), were digitally reconstructed using Imaris, and Fiji-ImageJ software. The resulting data analysis revealed that the territories of hippocampal astrocytes were significantly smaller, $19,373 \pm 1617 \mu\text{m}^3$, than those of IsoCx, $29,187 \pm 1648 \mu\text{m}^3$ (Figure 1c-iii, S9A, and S10A), while the size of the soma remained unchanged, $163.9 \pm 9.1 \mu\text{m}^3$ in IsoCx and $159.9 \pm 10.9 \mu\text{m}^3$ in Hipp (Mean \pm SEM), representing 0.6% and 0.9% of the astrocytic domain, respectively (Figure 1c-iv, S9B, S10A, and Table S4). Similarly, the quantity of major processes extending from the soma remained the same, 5 ± 0.4 for IsoCx astrocytes and 6 ± 0.5 for Hipp cells (Mean \pm SEM) (Figure 1c-v, and S9C).

To investigate astrocytic Ef as a subcompartment, a combination of tdTomato fluorescence with immunostaining was required (Figure 2). Figure 2a illustrates the co-staining of an astrocyte (gray, Figure 2a-i) with the proteins AQP-4 (green, Figure 2a-ii), and IB₄ (red, Figure 2a-iii). The goal was to visualize astrocytic Ef, highly polarized in AQP-4, and BVs through the endothelial expression of galactosyl residues recognized by IB₄. Although initially considered as two global and independent networks, their overlay revealed a tight localization and even some overlap between AQP-4 and IB₄ expression domains (Figure 2a-iv). Co-immunostaining images were processed using Imaris, Fiji-ImageJ, and Matlab, allowing for complete digital reconstructions of Ef in IsoCx and Hipp (representative example in Figure 2b-i), as well as analysis of their associated biophysical metrics

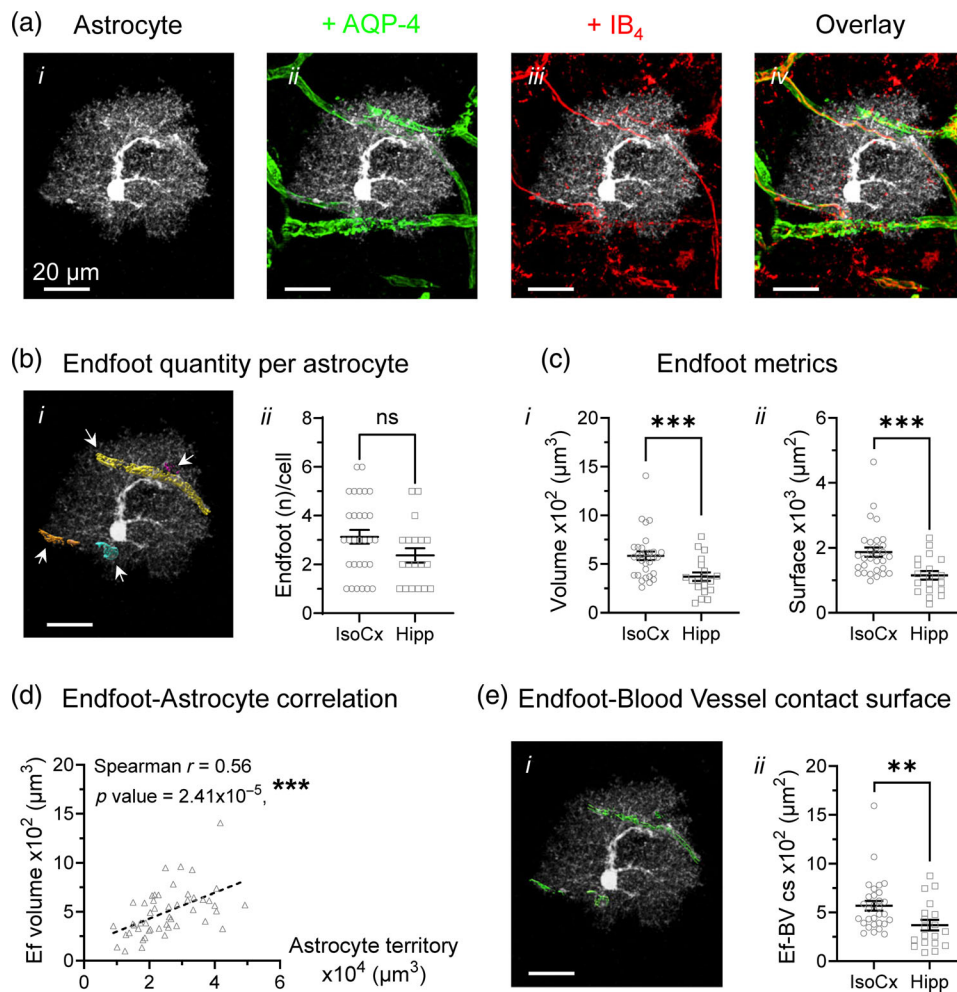


FIGURE 2 Morphological analysis of cortical and hippocampal astrocyte endfeet (Ef). (a) Representative tdTomato fluorescent cortical astrocyte (i). Examples of double immunostaining with AQP-4 (green) for visualization of Ef (ii) and with IB₄ (red) for visualization of endothelial cells lining the BVs (iii). Overlay image showing colocalization of astrocyte-AQP-4 and IB₄ (iv). (b) (i) Representative image of a cortical astrocyte with 3D digital reconstructions of its individual Ef indicated by white arrows (Ef 1: orange; Ef 2: light blue, Ef 3: yellow, and Ef 4: pink). (ii) Quantification of Ef per astrocyte in IsoCx and Hipp. (c) Analysis of Ef metrics, volume (i), and surface area (ii) in IsoCx and Hipp. (d) Spearman's correlation test between the Ef volume (x10², μm³) and astrocyte territories (x10⁴, μm³) (white triangles and dotted line). (e) (i) Representative image of a cortical astrocyte with 3D digital reconstructions of the Ef-BV contact surfaces (green). (ii) Analysis of the surface area (x10², μm²) in contact between Ef and BVs in IsoCx and Hipp. $n = 30$ astrocytes, $N = 7$ mice for IsoCx, $n = 19$ astrocytes, and $N = 5$ mice for Hipp. Data are presented as Mean ± SEM in IsoCx (white circles) and Hipp (white squares); *** $p < .001$; ** $p < .01$; ns $p > .05$; statistically tested by linear mixed models fit by restricted maximum likelihood, and Spearman correlation (Table S6). Scale bar = 20 μm.

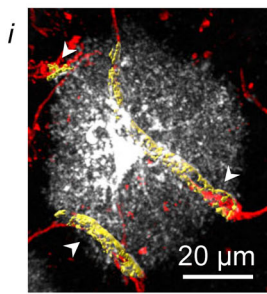
(Figures 2b–e, and S10). The number of Ef reported per astrocyte was quite similar between IsoCx, 3 ± 0.3 , and Hipp, 2 ± 0.3 (Mean ± SEM, Figures 2b-ii and S11A). However, the Ef volume was reduced to $370.3 \pm 43.4 \mu\text{m}^3$ in Hipp compared with $584.0 \pm 43.8 \mu\text{m}^3$ in IsoCx (Mean ± SEM, Figures 2c-i, S10A, and S11B). Similarly, the Ef surface area decreased from $1870 \pm 141.3 \mu\text{m}^2$ in IsoCx to $1151 \pm 129.8 \mu\text{m}^2$ in Hipp (Mean ± SEM, Figures 2c-ii, S10B, and S11C). Interestingly, Ef volumes and astrocyte territories were discovered to be positively correlated, with a Spearman's coefficient of 0.56, suggesting an interdependence between astrocyte size and the volume of its associated Ef (Figure 2d) (Dodge, 2008; Spearman, 1904).

The final biophysical metric calculated for Ef was the surface area of contact between Ef and BVs (Figure 2e). Consistent with the

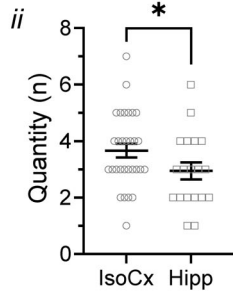
previously mentioned parameters, this value was reduced in Hipp at $369.9 \pm 53.9 \mu\text{m}^2$, compared with $568.8 \pm 48.9 \mu\text{m}^2$ in IsoCx (Mean ± SEM), representing 31.8% and 30.4%, respectively, or one-third, of the total Ef surface (Figures 2e-ii, S10, and S11D, and Table S4).

Further analysis of Ef–BV interactions allowed a more comprehensive characterization of the spatial organization of the gliovasculature units (Figure 3 and Table S5). The number of BVs per astrocyte was increased in IsoCx compared with Hipp, with 4 ± 0.2 and 3 ± 0.3 , respectively (Mean ± SEM) (Figures 3a-ii, and S12A). Similarly, in Figure 3a-iii, the frequency distribution revealed that 32% of Hipp astrocytes contacted 2 BVs (light gray bars), whereas 30% of IsoCx astrocytes interacted with 3 BVs (white bars). Figure 3a-i,b-i illustrate two types of structural organization between Ef and BVs. A single Ef

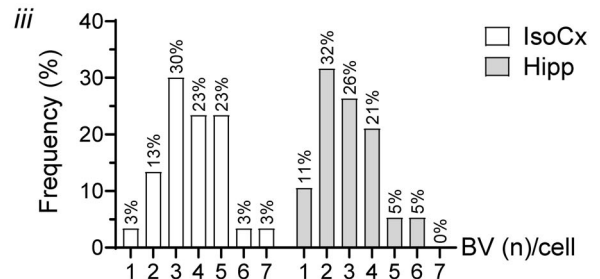
(a) Astrocyte + BV + Ef



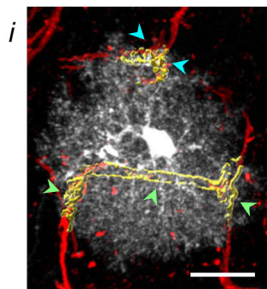
BV / astrocyte



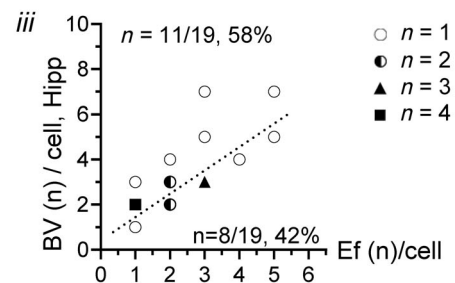
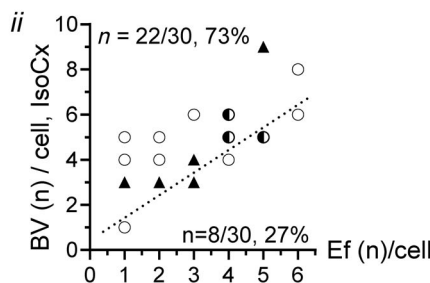
Frequency distribution



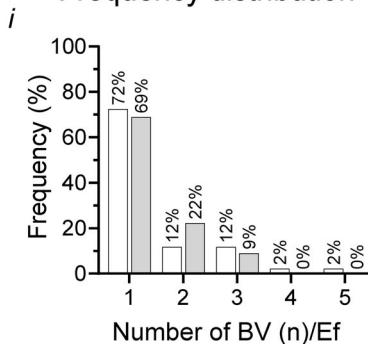
(b) Astrocyte + BV + Ef



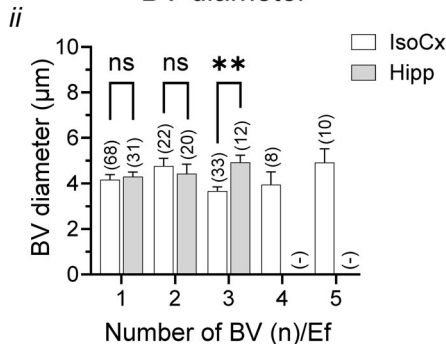
BV contacted by endfeet per astrocyte



(c) Frequency distribution



BV diameter



Ef-BV correlation

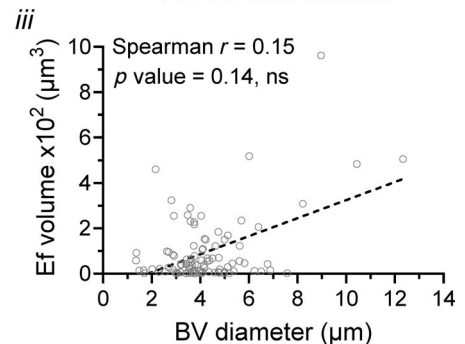


FIGURE 3 Blood vessels contacted by cortical and hippocampal astrocytes. (a) (i) Representative image of an astrocyte with 3D digital reconstructions of Ef (yellow) and BVs (red). Contact surfaces between Ef and BVs are indicated by white arrows. (ii) Quantification of BVs per astrocyte in IsoCx (white circles) and Hipp (white squares). (iii) Frequency distribution of the quantity of BVs contacted per astrocyte in IsoCx (white bars) and Hipp (light gray bars). (b) (i) Representative image of an astrocyte with 3D digital reconstructions of Ef (yellow) and BVs (red). Head arrows of the same color (cyan or green) indicate multiple BVs in contact with the same Ef. Quantity of Ef contacting one or more BVs per astrocyte in IsoCx (ii) and Hipp (iii). White circles: $n = 1$ astrocyte; half-filled circles: $n = 2$ astrocytes; black triangles: $n = 3$ astrocytes; black squares: $n = 4$ astrocytes. (c) (i) Frequency distribution of the quantity of BVs ensheathed per Ef in IsoCx (white bars) and Hipp (gray bars). (ii) BV diameter related to BV quantity ensheathed per Ef, (n) = number of BVs, in IsoCx (white bars) and Hipp (gray bars). (iii) Spearman's correlation test between Ef volume ($\times 10^2, \mu\text{m}^3$) and BV diameter (μm) (white circles, dotted line). $n = 30$ astrocytes, $N = 7$ mice for IsoCx, $n = 19$ astrocytes, $N = 5$ mice for Hipp. Data are presented as Mean \pm SEM; ** $p < .01$, * $p < .05$, ns $p > .05$, statistically tested by linear mixed models fit by restricted maximum likelihood, and Spearman correlation (Table S6). Scale bar = 20 μm .

can ensheath either a single or multiple BVs. In IsoCx, 73% of astrocytes had at least one Ef contacting more than one BV simultaneously, while only 27% exhibited a strict Ef-BV 1:1 ratio (Figure 3b-ii). In contrast, within Hipp, 58% of astrocytes had at least one Ef ensheathing more than 1 BV, while 42% maintained a 1:1 Ef:BV ratio (Figure 3b-iii). Analysis of the frequency distribution of the number of BVs ensheathed by each Ef revealed that in both IsoCx (white bars) and

Hipp (light gray bars), an Ef typically enwrapped a single BV, accounting for 72% and 69%, respectively (Figure 3c-i). Notably, there was no significant evidence that the diameter of the BVs affected the number of ensheathed vessels. Indeed, in the case of one BV per Ef, the mean BV diameter was $4.2 \pm 0.2 \mu\text{m}$ in IsoCx and Hipp; and for two BVs per Ef, $4.8 \pm 0.4 \mu\text{m}$ in IsoCx and $4.4 \pm 0.4 \mu\text{m}$ in Hipp (Mean \pm SEM). Interestingly, at three BVs per Ef, the BV diameter was observed to

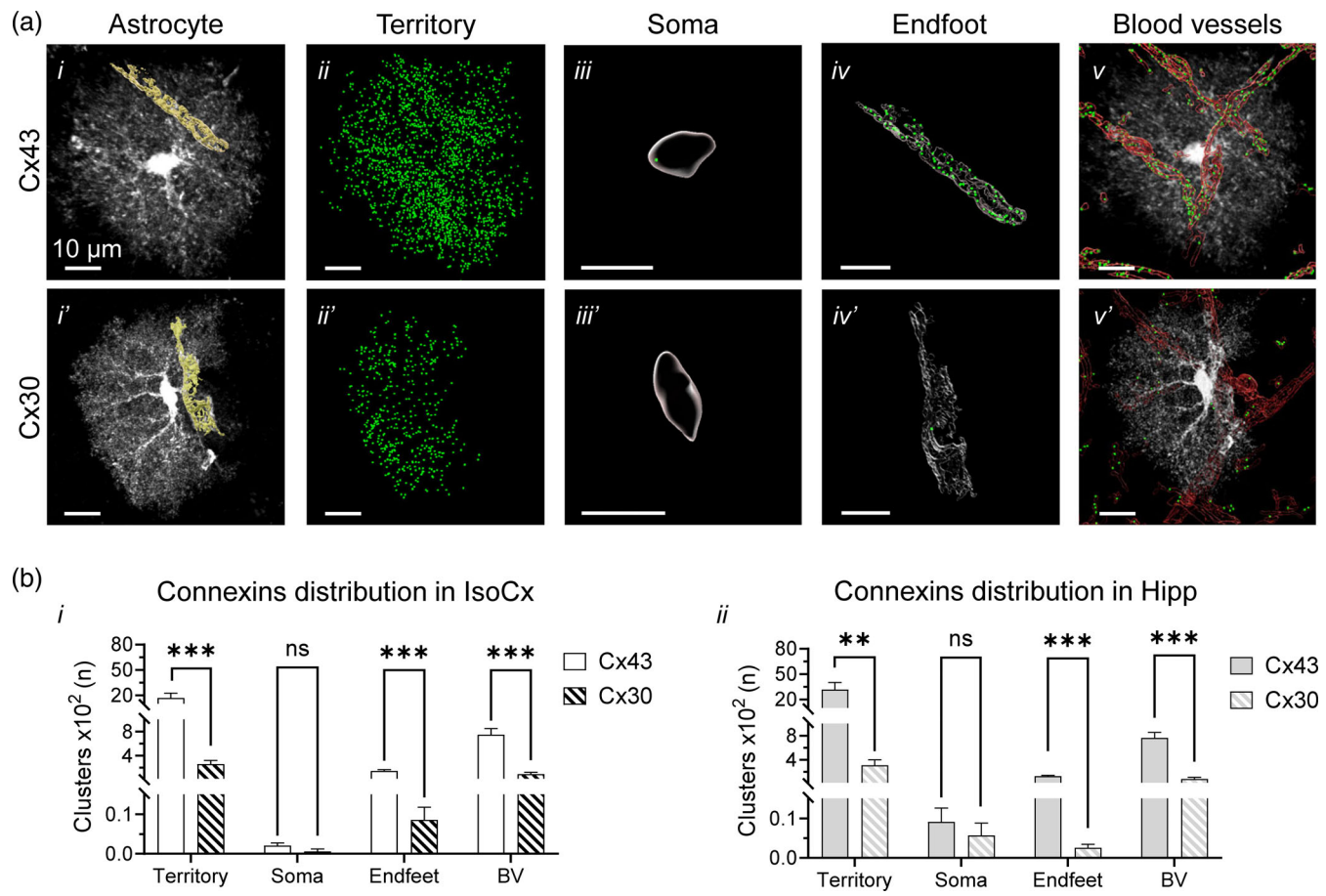


FIGURE 4 Connexin 43 and 30 cluster distributions. (a) (i) and (i') Representative images of astrocytes with 3D digital reconstructions of endfeet (Ef) (yellow). Digital spot detections (green dots) of Cx43 and Cx30 in astrocyte territory (A-ii and A-ii'), soma (A-iii and A-iii'), Ef (A-iv and A-iv'), and BVs (A-v and A-v'), respectively. (b) Absolute cluster distributions of Cx43 and Cx30 in astrocyte compartments and BVs in IsoCx (solid and striped white bars, respectively, i) and Hipp (solid and striped gray bars, respectively, ii). Cx43 data: $n = 10$ astrocytes, $N = 5$ mice for IsoCx and Hipp. Cx30 data: $n = 10$ astrocytes, $N = 5$ mice for IsoCx, and $n = 9$ astrocytes, $N = 5$ mice for Hipp. Data are presented as Mean \pm SEM; *** $p < .001$; ** $p < .01$; and ns $p > .05$, statistically tested by Wilcoxon and multiple linear regression analyses (Table S6). Scale bar = 10 μ m.

be smaller in IsoCx, $3.7 \pm 0.2 \mu$ m, versus $4.9 \pm 0.3 \mu$ m in Hipp (Mean \pm SEM, Figures 3c-ii, and S12B). Additionally, although some positive correlation between Ef volumes and BV diameters can be observed, the low Spearman's coefficient of 0.15 indicates only a weak relationship (Figure 3c-iii).

For a more thorough molecular characterization of astrocytes, co-immunostaining of tdTomato with AQP-4, IB₄, and either Cx43 or Cx30 (Figures S13 and S14, respectively) was performed in both IsoCx (Figures S13A and S14A) and Hipp (Figures S13B and S14B). Subsequently, the Imaris software was used to digitally detect Cx clusters in different compartments of interest, including the AT (Figure 4a-ii,a-ii'), soma (Figure 4a-iii,a-iii'), Ef (Figure 4a-iv,a-iv'), and BV network (Figure 4a-v, a-v'). The analysis, in absolute terms, of Cx clusters revealed an increasing distribution pattern from somas to Efs, BVs, and territories. These expression profiles were similar for both Cx43 (solid white and gray bars) and Cx30 (striped white and gray bars) in IsoCx (Figures 4b-i and S15) and Hipp (Figures 4b-ii and S16). Interestingly, within the same brain area, in both IsoCx and Hipp, Cx43 clusters consistently exhibited the highest expression compared with

Cx30. Specifically, for Cx43 clusters, the expression levels per compartment in IsoCx were as follows: astrocyte territories 1694 ± 568 , BVs 746 ± 103 , Ef 145 ± 22 , and soma 2 ± 1 (Mean \pm SEM, solid white bars, Figures 4b-i and S15). In Hipp, the expression levels of the clusters, in the same order, were as follows: 3166 ± 844 , 764 ± 90 , 126 ± 15 , 9 ± 4 (Mean \pm SEM) (solid gray bars, Figures 4b-ii and S16). In contrast, for Cx30 clusters in IsoCx, the expression levels per compartment were: AT 256 ± 62 , BVs 92 ± 28 , Ef 9 ± 3 , and soma 1 ± 1 (Mean \pm SEM, striped white bars, Figures 4b-i and S15). In Hipp, the expression levels of the clusters, in the same order, were as follows: 306 ± 94 , 79 ± 28 , 3 ± 1 , and 6 ± 3 (Mean \pm SEM, striped gray bars, Figures 4b-ii and S16).

Because of the obvious substantial volume disparities between each compartment (Table S3), analyses of Cx43 and Cx30 densities were essential to facilitate a meaningful and normalized comparison of the expression and distribution of these two proteins (Figure 5). In this regard, the volume densities of Cx43 and Cx30 clusters were first analyzed (Figure 5a, S17 and S18). Notably, Figure 5a-i shows that Ef in IsoCx overexpressed both Cxs, with 0.64 ± 0.17 particles per μ m³

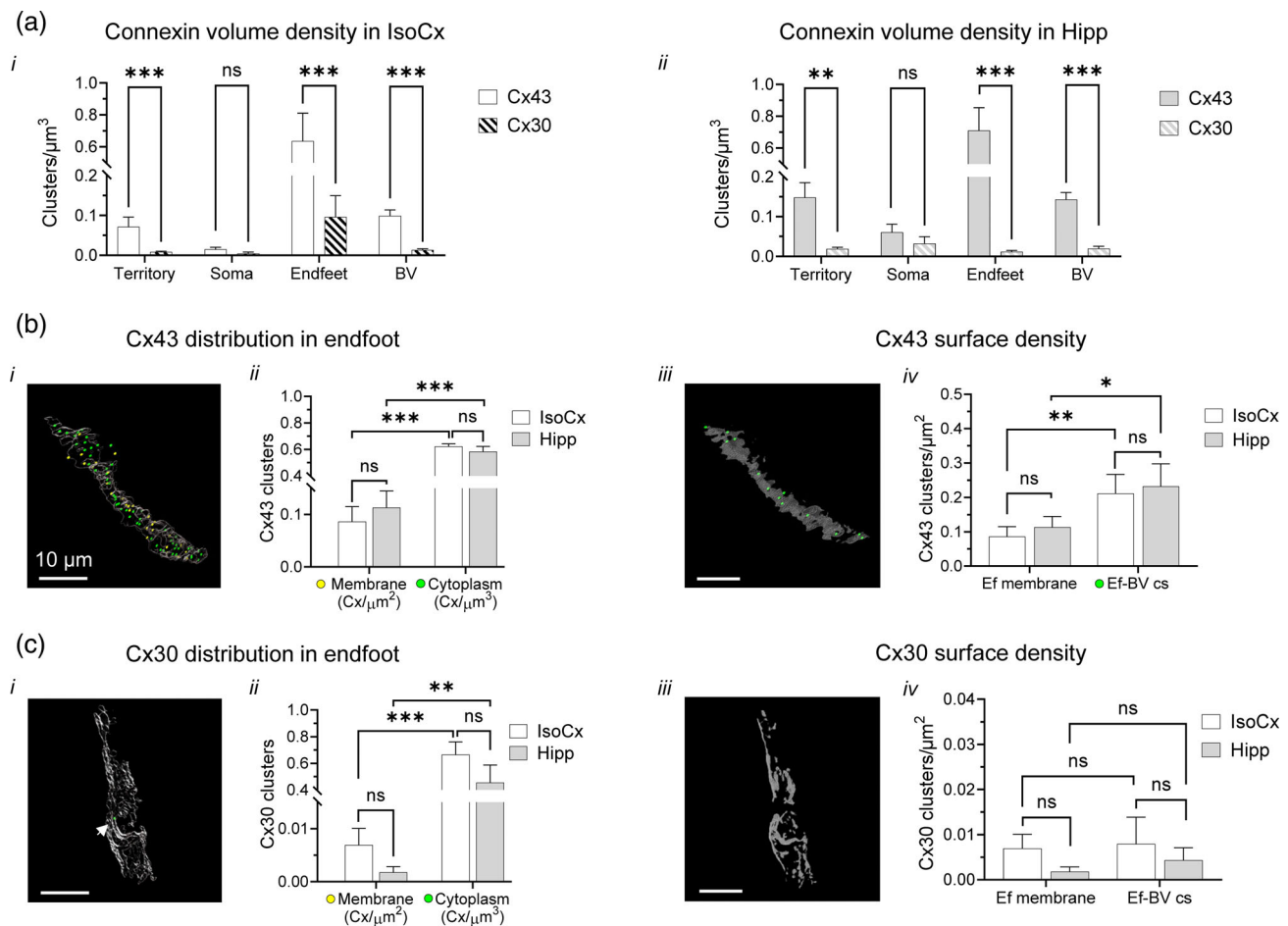


FIGURE 5 Connexin 43 and 30 density distributions. (a) Volume density of Cx43 and Cx 30 clusters in each astrocyte compartment and BVs in IsoCx (solid white, and striped white bars, respectively, i) and Hipp (solid gray and striped gray bars, respectively, ii). (b and c) (i) Digital representations of Ef (soap bubble design) with Cx43 (B-i) and Cx30 (C-i) clusters at the plasma membrane (yellow dots) and in the cytoplasm (green dots, for Cx30 indicated by a white arrow). Cluster densities of Cx43 (B-ii) and Cx30 (C-ii) at the Ef plasma membrane (yellow dots, surface density, clusters/ μm^2), and in the Ef cytoplasm (green dots, volume density, clusters/ μm^3). (b and c) (iii) Digital reconstructions of Ef-BV cs (gray) with Cx43 (B-iii) and Cx30 (C-iii) clusters (green spots). Surface densities of Cx43 (B-iv) and Cx30 (C-iv) clusters at Ef membrane and Ef-BV cs (clusters/ μm^2) in IsoCx (white bars) and Hipp (light gray bars). Cx43 data: $n = 10$ astrocytes, $N = 5$ mice for IsoCx and Hipp. Cx30 data: $n = 10$ astrocytes, $N = 5$ mice for IsoCx, and $n = 9$ astrocytes, $N = 5$ mice for Hipp. Data are presented as Mean \pm SEM; *** $p < .001$; ** $p < .01$; * $p < .05$ and ns $p > .05$, statistically tested by Wilcoxon tests, multiple linear regression analyses, linear mixed models fit by restricted maximum likelihood, and paired t -tests (Table S6). Scale bar = 10 μm .

for Cx43 (solid white bars) and 0.10 ± 0.05 for Cx30 (striped white bars, Mean \pm SEM). In contrast, Cx densities in all other compartments were lower for Cx43 as follows: 0.07 ± 0.02 in territory, 0.02 ± 0.01 in soma, and 0.10 ± 0.02 in BVs (particles per μm^3 , Mean \pm SEM, solid white bars, Figures 5a-i and S17). For Cx30, the densities in the other compartments were 0.010 ± 0.002 in territory; 0.004 ± 0.004 in soma; and 0.010 ± 0.004 in BVs (particles per μm^3 , Mean \pm SEM, striped white bars, Figures 5a-i and S17). Similarly, in Hipp, Figure 5a-ii shows that Ef contained an increased expression of Cx43 clusters with 0.71 ± 0.14 particles per μm^3 (light gray bars, Mean \pm SEM), comparable to the value calculated in IsoCx (Figure 5a-i). Again, Cx43 density was consistently lower in other compartments, as follows: 0.15 ± 0.04 in territory; 0.06 ± 0.02 in soma; and 0.14 ± 0.02 in BVs (particles per μm^3 , Mean \pm SEM, solid gray bars, Figures 5a-ii and S18). However, for Cx30, Hipp density was not increased in Ef

compared with the other compartments with 0.011 ± 0.004 particles per μm^3 versus 0.019 ± 0.005 in territory; 0.03 ± 0.02 in soma; and 0.019 ± 0.006 in BVs (striped gray bars, Mean \pm SEM, Figures 5a-ii and S18). In summary, a marked overexpression of both proteins was observed in Ef compared to other compartments. Cx43 was found to be 10 and 6 times more abundant in IsoCx and Hipp, respectively, while Cx30 was 11 times more expressed, albeit only in the Ef of cortical astrocytes.

Subsequently, Cx43 and Cx30 cluster densities were analyzed specifically in Ef (Figure 5b,c). Figure 5b-i,c-i depict representative examples of Cx43 and Cx30 proteins differentially distributed between the Ef membrane (yellow dots) and cytoplasm (green dots). Distribution analysis revealed a similar level of expression between the two Cxs in the Ef cytoplasm with 0.62 ± 0.02 Cx43 and 0.67 ± 0.10 Cx30 per μm^3 in IsoCx (white bar); and 0.58 ± 0.04 Cx43 and

0.46 ± 0.13 Cx30 per μm^3 in Hipp (light gray bar, Mean \pm SEM, Figures 5b-ii,c-ii and S20). In contrast, lower surface densities were found at the Ef membrane with 0.09 ± 0.03 and 0.11 ± 0.03 Cx43 clusters per μm^2 ; and 0.007 ± 0.003 and 0.002 ± 0.001 Cx30 clusters per μm^2 , in IsoCx and Hipp, respectively (white and light gray bars, Mean \pm SEM, Figures 5b-ii,c-ii, S19, and S20). Regarding Ef–BV cs, 0.21 ± 0.06 and 0.23 ± 0.07 Cx43 clusters per μm^2 were expressed in IsoCx and Hipp (white and light gray bars, respectively, Mean \pm SEM, Figures 5b-iv and S21), whereas Cx30 clusters were significantly scarcer or even absent in both brain areas, with 0.008 ± 0.006 and 0.004 ± 0.003 clusters per μm^2 in IsoCx and Hipp (white and light gray bars, respectively, Mean \pm SEM, Figures 5c-iv and S22). These distinct profiles highlight a large pool of Cxs in the Ef cytoplasm. Although we observed a higher apparent intensity of the Cx43 signal at the interface with BVs, precise localization to the interface cannot be concluded due to the limitations of the immunostaining technique.

4 | DISCUSSION

This study explores the intricate biophysical architecture and molecular organization of astrocytes, with a particular focus on their Ef connections to the vasculature within the mouse IsoCx and Hipp (Batiuk et al., 2020; Bayraktar et al., 2020; Endo et al., 2022; Lanjakornsiripan et al., 2018; Salmon et al., 2023; Viana et al., 2023). These brain regions are of great interest due to their central role in cognitive task performance and memory consolidation (Lawal et al., 2022; Refaeli et al., 2021; Wang et al., 2022), making them vulnerable to neuropathologies such as Alzheimer's disease (Planche et al., 2022), amyotrophic lateral sclerosis (Zhou et al., 2016), and major depressive disorder (Zhang et al., 2018). It should be noted that we do not consider anatomical subfields within brain areas, or cell organization in layers.

The results indicate that astrocytes in both brain regions have comparable soma sizes and a similar number of major processes and Ef. However, distinctive features emerge in hippocampal astrocytes compared to their isocortical counterparts. Specifically, hippocampal cell territories appear smaller with reduced Ef dimensions, including length, width, volume, surface area, and contact surface with BVs. Thus, our results reveal two levels of morphological complexity in astrocytes: a macroscopic level characterized by heterogeneities in domain size, and a microscopic level defined by reduced Ef metrics that strongly correlate with cell dimensions. Nevertheless, the consistent number of Ef and major processes observed in both brain areas, despite territorial dimensional constraints, suggests a conserved process of branch arborization. These results are in line with and complement a recent study by Viana et al., which found that the volume fraction of leaflets and AT dimensions are independent, suggesting distinct molecular regulation of these two architectural features (Viana et al., 2023).

These findings raise several intriguing questions. For instance, while the number of major branches appears constant, does the density of leaflet arborization mirror this stability, or does it adjust relative

to the territory volume occupied by the astrocytes? Further work using electron microscopy could characterize and compare the nanoscopic ultrastructure of astrocytic arborization between cells across brain areas (Aten et al., 2022). It is conceivable that smaller cells may develop fewer fine processes within a limited domain volume. This raises the question of whether hippocampal astrocytes have reduced functionalities due to fewer interactions with neurons, oligodendrocytes, or other astrocytes. Previous studies have shown that the proximity of astrocytes to other cells manages their spectrum of actions, rather than their strict physical dimensions. Indeed, in the cornu ammonis 1 lamina (CA1), astrocytes were observed to harbor larger neuronal populations within their territories. Regardless of process length, their proximity to the pyramidal layer facilitates enhanced contacts with neurons and could potentially modulate their functionalities (Aten et al., 2022; Refaeli et al., 2021). Moreover, considering the key role of Ef in pivotal physiological mechanisms, including BBB maintenance, regulation of cerebral blood flow, and nutrient (cyclic AMP, InsP_3 , Ca^{2+} , and amino acids)/waste (CO_2) exchange (Cibelli et al., 2021; Díaz-Castro et al., 2023; Giaume et al., 2010; Kubotera et al., 2019; Obermeier et al., 2013; Weber & Barros, 2015), we wonder whether the revealed reduced contact surfaces between Ef and BVs in Hipp influence metabolic trafficking between the brain and systemic circulation. Given these physical constraints, how do hippocampal astrocytes meet their metabolic demands to maintain local homeostasis? Astrocytes could respond by increasing the expression of specialized proteins, such as transporters, ion channels, and Cxs, at the Ef membrane, or they could have geometry and nanostructural adaptations, as demonstrated in previous studies. Indeed, the size and shape of mitochondria have been observed to vary significantly between astrocytic subcompartments to meet metabolic demands (Aten et al., 2022; Salmon et al., 2023). Thus, the higher density of astrocytes in Hipp (Keller et al., 2018; Olude et al., 2015) could compensate for the reduced Ef in quantity and dimension through intensive molecule transports across the BBB, which would then diffuse through the extensive astrocytic network via GJs (Hösl, Binini, et al., 2022).

To better understand the biophysical and molecular organization of Ef, we first investigated their detailed anatomical interactions with cerebral BVs within NGV units. In IsoCx, our study shows that the majority of astrocytes contact three BVs, with potential interactions extending to seven, whereas in Hipp, astrocytes engage with only two to six vessels. This difference could be attributed to the lower vascular density in Hipp, which reduces the probability of cell connections with BVs (Hösl, Zuend, et al., 2022). Nevertheless, we highlight that a significant proportion of astrocytes in both regions, 73% in IsoCx and 58% in Hipp have at least one Ef contacting multiple BVs simultaneously. However, the majority of Ef, 72% and 69% (IsoCx and Hipp, respectively), tend to enwrap individual vessels, as illustrated in Figure 6. Taken together, these results suggest a new property of astrocytes, a kind of “plasticity,” in which cells can generate Ef that ensheath one or more vessels concurrently and independent of BV diameters. Interestingly, we also discovered that only 30% of the Ef surface directly interacts with the endothelial cells lining the walls of

BVs. This implies that 70% of the Ef membrane may communicate directly with the extracellular brain space, possibly through proteins such as Cx hemichannels or pannexins (Giaume et al., 2013). Overall, our anatomical vascular analysis is consistent with the concept of a flexible gliovascular network, tailored for specific functions and adapted to local environmental demands. Nevertheless, further investigations with advanced technologies are needed to better understand the functional dynamics of Ef, especially in Hipp (Alonso-Gardón et al., 2021; Baldwin et al., 2023; Díaz-Castro et al., 2023; Stokum et al., 2021). Indeed, it would be of great interest to determine whether astrocytes can generate new Ef, which would contact one or multiple BVs under certain circumstances, in the same way that reactive or restored astrocytes generate more fine processes (Rodríguez et al., 2013; Yang et al., 2024).

Astrocytes are densely interconnected by GJs to form a broader network, critical for facilitating the diffusion of essential compounds to brain cells across regions (Boulay, Saubaméa, et al., 2015; Ezan et al., 2012; Huang et al., 2021; Rouach et al., 2008; Simard et al., 2003). The protein ratio predominantly favored Cx43 across the AT, Ef, and BVs, underscoring the pivotal role of this protein under physiological conditions.

Despite potential estimation challenges of Cxs due to the nanoscale properties of the finest astrocytic extensions involved in synapses or cell–cell interactions, which are only detectable by techniques such as electron microscopy (Heller & Rusakov, 2019), we believe that the final analysis was not affected. Indeed, Ef volumes are hundreds of cubic microns and therefore large enough to be examined with confocal microscopy, as evidenced by this and other works (Wang et al., 2021; Zisis et al., 2021). It is clear that the Cx distribution maps to the Ef, including its cytoplasm and the plasma membrane, and the interface with the BV in both IsoCx and Hipp. Notably, both Cxs were primarily stored in the cytoplasm rather than at the Ef plasma membrane, indicating a strategic arrangement to potentially respond rapidly to fluctuating metabolic demands (Figure 6). Thus, during periods of increased requirements or pathological conditions, additional Cxs could be mobilized to the cell surface or retained in the Ef cytoplasm as a reserve pool in cases of nominal basal needs.

Although the results hint at higher expression of Cx43 at the Ef membrane in contact with the BVs, we cannot conclude this with certainty since immunolabeling experiments cannot definitively show direct interactions between molecules. In particular, Cxs-mediated GJs could also belong to the Ef of neighboring astrocytes that do not express tdTomato and connect cells to rapidly spread molecules in a communication network (El-Khoury et al., 2006; Huang et al., 2021; Katoozi et al., 2017; Langer et al., 2017). Therefore, further complementary investigations are required to accurately localize and quantify Cx43 proteins at the Ef–BV interface. Our findings detected the colocalization of Cxs, Ef, and BVs based on their respective immunostaining, and similar to Cibelli and colleagues, both Cxs and AQP-4 were found in perivascular Ef (Cibelli et al., 2021).

It is interesting to consider the potential implications of Cx43 localization. It would be consistent with a critical exchange function of this protein with systemic circulation, especially given that Cx43 was

already found in the endothelial cells of vessel walls, where they are theoretically able to establish GJs with adjacent cells (Errede et al., 2002; Genet et al., 2023; Liang et al., 2020).

In contrast, Cx30 globally showed lower protein levels and were not overexpressed in the Ef of hippocampal astrocytes compared to isocortical counterparts with a sparse and uniform distribution at the Ef membrane. These results align with previous studies reporting variation in Cx levels across different brain regions, such as lower Cx30 expression in the stratum radiatum of control mice (Belousov et al., 2017; Boulay, Mazeraud, et al., 2015; Cibelli et al., 2021; Huang et al., 2021; Rouach et al., 2008; Söhl et al., 2004; Theofilas et al., 2017). Some theorize that Cx30 is a highly fluid isoform with the ability to rapidly rearrange GJ plaques, whereas Cx43 is a more immobile isoform (Cibelli et al., 2021; Stout et al., 2015). Thus, Cx30 may be an additional tool by which astrocytes respond to molecular requirements in a region-specific manner. Furthermore, it is worth noting that some Ef may have dimensions falling below the resolution limit of the confocal microscope, restricting accurate Cx characterizations as done during our work. Hence, we advocate for further investigations using cutting-edge technologies, such as super-resolution microscopy, to overcome such technical limitations.

Collectively, these results reinforce the concept of astrocytic processes and Ef as functionally autonomous microdomains, as suggested by some studies (Agarwal et al., 2017; Holt, 2023), capable of regulating their physiology based on local demands, particularly in different brain regions.

Under healthy conditions, the glia-vasculature (GV) unit consists of an astrocyte (light blue) that interacts with the surrounding BVs (red) through its Ef. As illustrated on the left, an astrocyte can establish multiple contacts with several BVs with different Ef (Endfeet 1 and 2), or/and can ensheath several BVs with the same Ef (Endfoot 3). Notably, only 30% of the Ef surface is involved in these types of interactions with the endothelial cells lining the BV walls (green line on the left and green dotted line on the right), suggesting that the remaining 70% could directly exchange with the extracellular brain space. To better characterize the GV interactions, further molecular experiments in this study investigated the overall expression and distribution patterns of Cx43 and Cx30 in isocortical and hippocampal astrocytes, including their associated Ef compartments (right). As displayed on the right, although astrocytes exhibit a higher expression of Cx43 than Cx30, both proteins are abundantly stored in the Ef cytoplasm rather than at the plasma membrane (surface).

While our study provides valuable insights, it is noteworthy to acknowledge several limitations inherent to our methodology:

1. Partial cell population targeting: In our project, only sparse fluorescent astrocytes were used to investigate single-cell morphology and their interactions with the vasculature. To induce tdTomato labeling, the GFAP promoter, the most common genetic sequence found in the majority of CNS astrocytes was used to control tdTomato transgene expression (Jurga et al., 2021; Nolte et al., 2001; Preston et al., 2019). However, the entire cell population does not carry this promoter, which to some extent introduces a selectivity

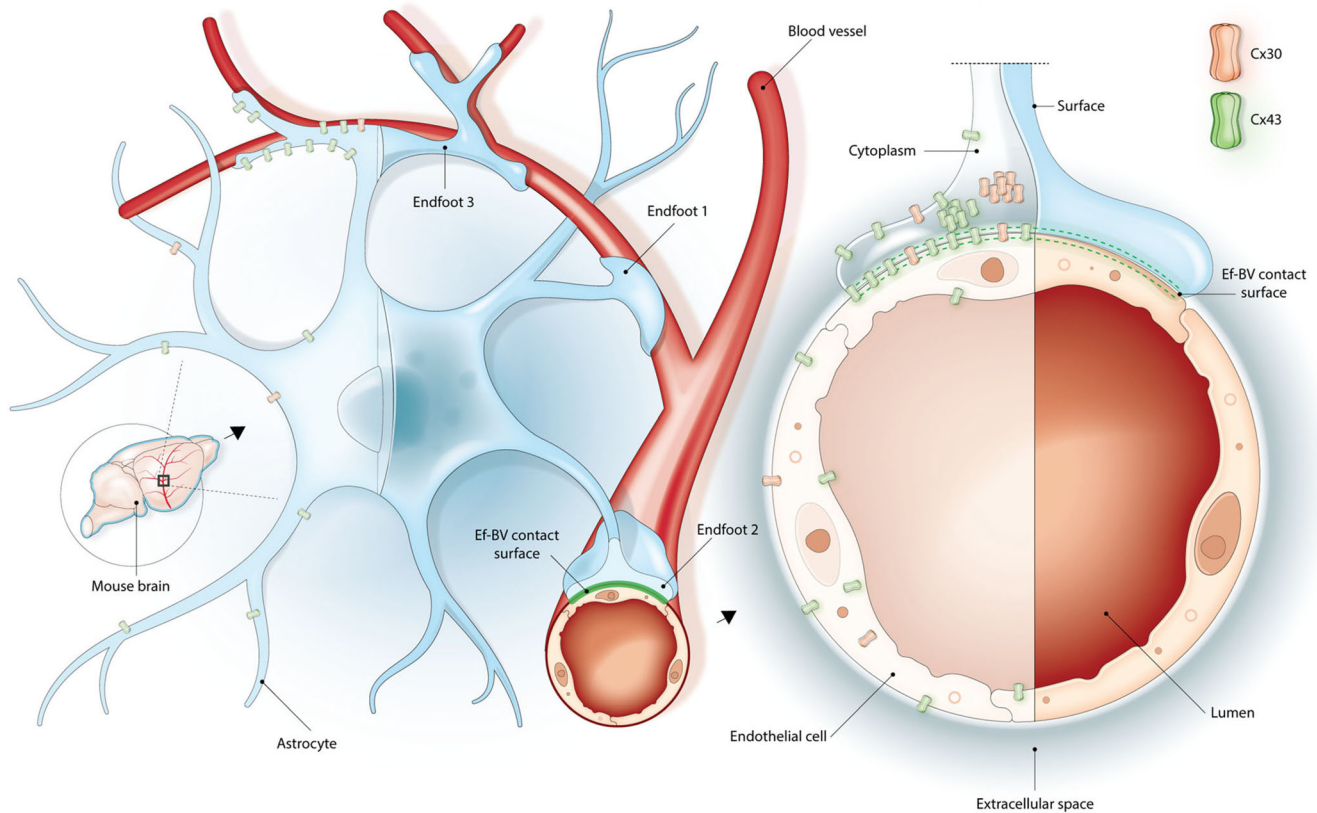


FIGURE 6 Schematic models of the glia-vasculature architecture with connexin distribution and density. Under healthy conditions, the glia-vasculature (GV) unit consists of an astrocyte (light blue) that interacts with the surrounding BVs (red) through its Ef. As illustrated on the left, an astrocyte can establish multiple contacts with several BVs with different Ef (Endfeet 1 and 2), or/and can ensheath several BVs with the same Ef (Endfoot 3). Notably, only 30% of the Ef surface is involved in these types of interactions with the endothelial cells lining the BV walls (green line on the left and green dotted line on the right), suggesting that the remaining 70% could directly exchange with the extracellular brain space. To better characterize the GV interactions, further molecular experiments in this study investigated the overall expression and distribution patterns of Cx43 and Cx30 in isocortical and hippocampal astrocytes, including their associated Ef compartments (right). As displayed on the right, although astrocytes exhibit a higher expression of Cx43 than Cx30, both proteins are abundantly stored in the Ef cytoplasm rather than at the plasma membrane (surface).

bias of astrocytes to be considered in our analyses and interpretations. Notably, two other genetic promoters, *S100 β* and *ALDH1L1*, are also prevalent in the literature, but again, neither is universal across the entire population of astrocytes and has other caveats, such as detection in some other brain cells or age-dependent expression (Preston et al., 2019). To enhance the reliability of our results, we performed *ALDH1L1* immunostaining on brain slices containing tdTomato fluorescence (Figure S7B). Colocalization was observed between the two, confirming, with the recorded electrophysiological data, the cell identity as astrocyte (Figures S7B-iii and S3). Furthermore, we noted neighboring astrocytes expressing only *ALDH1L1*, attesting to the difficulty of targeting the entire astrocyte population with either marker, tdTomato, or *ALDH1L1* alone (Figure S7B-ii).

2. Tissue fixation challenges: Our study required the use of chemically fixed brain slices, which posed a risk of tissue integrity alterations. To minimize physical distortions of brain areas, extracellular space, cells, Ef swelling, or Ef membrane detached from BVs, we preferred a slight PFA fixation (Hösl, Zuend, et al., 2022; Idziak

et al., 2023; Korogod et al., 2015). Anatomical damages could affect the accuracy of various measurements, including astrocyte territories and Ef dimensions. With this fixation method, some measured parameters, such as the volume of AT and soma, as well as the number of cell-BV interactions remained similar to those found in the literature using other techniques like transcatheter perfusion, confirming a well-preserved architecture of the tissue (Hösl, Zuend, et al., 2022; Kalisvaart et al., 2023; Moye et al., 2019). Moreover, a brief PFA incubation prevented tdTomato fluorescence quenching, which is observed during other typical protocols such as overnight fixation, transcatheter perfusion, tissue clearing, and cryo-slicing (Tang et al., 2021).

3. Antibody diffusion, nonspecific staining, and autofluorescence: To achieve comprehensive imaging of entire astrocytes, including their processes and Ef in 3D, we used brain slices that were 150- μ m-thick. However, the sample thickness appeared as a physical barrier, which limited the deep antibody diffusion and resulted in incomplete stainings. To address this constraint, we used Triton X-100 to permeabilize the biomembranes (Mattei et al., 2017).



When available, conjugated primary antibodies were applied to reduce the number of products to diffuse, and when not, nanoantibodies were preferred to facilitate tissue penetration (Pedre  n  ez et al., 2021). In addition, prolonged incubations of highly concentrated antibodies were performed at RT to further facilitate tissue penetration. Despite these efforts, nonspecific stainings and autofluorescence can increase the risk of signal misanalysis and misinterpretation (Sakr et al., 2023). Therefore, in all immunostaining steps, a NGS-based solution was primarily used to block as many nonspecific and reactive sites of the samples as possible. In addition, the penetration of each antibody was evaluated across the tissue depth, in IsoCx and Hipp (Figures S5 and S6). It is important to note that fluorescence intensities decreased due to two main factors: the physical barrier imposed by brain tissue thickness, as previously explained, and the absence of protein expression, which results in no signal. Finally, through analysis of negative controls and multiple images, we confirmed that signal intensities were sufficient for detection by Imaris software, both inside and around the targeted astrocytes, even in deep areas.

4. Microscopy limitations: Astrocytic processes can have diameters as thin as 50–100 nm, which is below the diffraction limit of conventional light microscopy (200–300 nm) (Heller & Rusakov, 2019). Therefore, during astrocyte image acquisition, it cannot be excluded that some processes were missed, which could skew the correct assessment of cell territories. Combining other cutting-edge technologies, such as super-resolution microscopy, may help overcome this limitation (Cibelli et al., 2021; Smith & Verkman, 2015).
5. Software-based analysis: Imaris, Fiji-ImageJ, and Matlab software were used to detect and model astrocytes, Ef, BVs, and Cxs. However, as explained above, even when minimized, nonspecific signals and background noise are still present and can be digitally recognized as true cell components. To avoid at most false positives, negative control experiments were consistently performed by a trained experimenter to challenge and validate immunostaining protocols as well as microscopy acquisition and image processing parameters to ensure the most consistent and relevant results.

In conclusion, our study sheds light on the structural and molecular organization of astrocytes and their Ef. These findings not only deepen our understanding of astrocyte biology but also potentially inform new approaches for treating neurological disorders or brain injuries. Moreover, while hippocampal astrocytes exhibit smaller territories compared with their isocortical counterparts, their process arborizations remain independent, suggesting complex regulatory mechanisms. We also uncovered a remarkable structural heterogeneity of Ef, where a single astrocyte can have multiple Ef, each surrounding a single or multiple vascular branches simultaneously. This intriguing versatility hints at underlying molecular features that warrant further investigations, particularly regarding their role in brain homeostasis and response to pathological conditions. Our study also characterized the composition and the density of Cx proteins. While Cx43 and Cx30 were detected as expected in whole astrocytes from

both brain areas, we demonstrated for the first time an overexpression of these proteins in the Ef. These findings underscore the critical role of these two isoforms in the complex crosstalk between the brain and systemic blood circulation. Notably, a persistent and more pronounced Cx43 expression was observed, suggesting a minor role for Cx30 under physiological conditions. Moreover, both proteins were predominantly localized in the Ef cytoplasm rather than at the plasma membrane, suggesting a protein reservoir readily mobilized in response to increased metabolic demands or pathological conditions. Collectively, our results provide new insights into the structural and molecular complexity of astrocytes, and make a valuable contribution to our fundamental understanding of these glial cells. Finally, these findings are potentially useful for large-scale brain modeling of the NGV and prompt the exploration of intriguing concepts, such as astrocyte plasticity similar to that of neurons, which opens up exciting avenues for future investigation.

AUTHOR CONTRIBUTIONS

CL, RG, NC, and DK: Investigations and writing. CL, RG, NC, GA, and DK: Data collection, statistical analysis, and literature review. CL, RG, NC, EB, MA: Figures design. CL, HM and DK: Supervision. All authors contributed to the article and approved the submitted version.

ACKNOWLEDGMENTS

We thank Monica Favre for her help in the early stage of the study, Rodrigo Perin and Emmanuelle Logette for their advice on the experiments and analyses; the PhenoGenomics Center of EPFL, and especially Rapha  l Doenlen for animal care, advice, and technical assistance; Marion Leleu for her advice on the statistical analyses; Julie Meystre and Deborah La Mendola for technical support with the mouse genotyping and animal license. Additional thanks go to Karin Holm for editing support.

FUNDING INFORMATION

This study was supported by funding to the Blue Brain Project, a research center of the   cole Polytechnique F  d  rale de Lausanne (EPFL), from the Swiss government's ETH Board of the Swiss Federal Institutes of Technology. The funders had no role in study design, data collection, and analysis, decision to publish, or preparation of the manuscript.

CONFLICT OF INTEREST STATEMENT

The authors declare that the research was conducted in the absence of any commercial or financial relationships that could be construed as a potential conflict of interest.

DATA AVAILABILITY STATEMENT

The data that support the findings of this study are openly available on Zenodo at <https://doi.org/10.5281/zenodo.8155041>.

ORCID

Charlotte Lorin  <https://orcid.org/0000-0001-6424-4504>

Romain Guet  <https://orcid.org/0000-0001-6715-4897>

REFERENCES

- Abbott, N. J., Rönnbäck, L., & Hansson, E. (2006). Astrocyte–endothelial interactions at the blood–brain barrier. *Nature Reviews Neuroscience*, 7(1), 41–53. <https://doi.org/10.1038/nrn1824>
- Abdellah, M., Cantero, J. J. G., Guerrero, N. R., Foni, A., Coggan, J. S., Cali, C., Agus, M., Zisis, E., Keller, D., Hadwiger, M., Magistretti, P. J., Markram, H., & Schürmann, F. (2023). Ultraliser: A framework for creating multiscale, high-fidelity and geometrically realistic 3D models for in silico neuroscience. *Briefings in Bioinformatics*, 24(1), bbac491. <https://doi.org/10.1093/bib/bbac491>
- Abdellah, M., Foni, A., Zisis, E., Guerrero, N. R., Lapere, S., Coggan, J. S., Keller, D., Markram, H., & Schürmann, F. (2021). Metaball skinning of synthetic astroglial morphologies into realistic mesh models for in silico simulations and visual analytics. *Bioinformatics*, 37-(Supplement_1), i426–i433. <https://doi.org/10.1093/bioinformatics/btab280>
- Agarwal, A., Wu, P.-H., Hughes, E. G., Fukaya, M., Tischfield, M. A., Langseth, A. J., Wirtz, D., & Bergles, D. E. (2017). Transient opening of the mitochondrial permeability transition pore induces microdomain calcium transients in astrocyte processes. *Neuron*, 93(3), 587–605.e7. <https://doi.org/10.1016/j.neuron.2016.12.034>
- Agre, P. (1997). Molecular physiology of water transport: Aquaporin nomenclature workshop. Mammalian aquaporins. *Biology of the Cell*, 89(5–6), 255–275. <https://doi.org/10.1111/j.1768-322X.1997.tb01021.x>
- Allen, N. J., & Lyons, D. A. (2018). Glia as architects of central nervous system formation and function. *Science*, 362(6411), 181–185. <https://doi.org/10.1126/science.aat0473>
- Alonso-Gardón, M., Elorza-Vidal, X., Castellanos, A., La Sala, G., Armand-Ugon, M., Gilbert, A., Di Pietro, C., Pla-Casillan, A., Ciruela, F., Gasull, X., Nunes, V., Martínez, A., Schulte, U., Cohen-Salmon, M., Marazziti, D., & Estévez, R. (2021). Identification of the GlialCAM interactome: The G protein-coupled receptors GPRC5B and GPR37L1 modulate megalencephalic leukoencephalopathy proteins. *Human Molecular Genetics*, 30(17), 1649–1665. <https://doi.org/10.1093/hmg/ddab155>
- Aten, S., Kiyoshi, C. M., Arzola, E. P., Patterson, J. A., Taylor, A. T., Du, Y., Guiher, A. M., Philip, M., Camacho, E. G., Mediratta, D., Collins, K., Boni, K., Garcia, S. A., Kumar, R., Drake, A. N., Hegazi, A., Trank, L., Benson, E., Kidd, G., ... Zhou, M. (2022). Ultrastructural view of astrocyte arborization, astrocyte–astrocyte and astrocyte–synapse contacts, intracellular vesicle-like structures, and mitochondrial network. *Progress in Neurobiology*, 213, 102264. <https://doi.org/10.1016/j.pneurobio.2022.102264>
- Attene, M. (2010). A lightweight approach to repairing digitized polygon meshes. *The Visual Computer*, 26(11), 1393–1406. <https://doi.org/10.1007/s00371-010-0416-3>
- Baldwin, K. T., Murai, K. K., & Khakh, B. S. (2023). Astrocyte morphology. *Trends in Cell Biology*, 34, 547–565. <https://doi.org/10.1016/j.tcb.2023.09.006>
- Batiuk, M. Y., Martirosyan, A., Wahis, J., De Vin, F., Marneffe, C., Kusserow, C., Koeppen, J., Viana, J. F., Oliveira, J. F., Voet, T., Ponting, C. P., Belgard, T. G., & Holt, M. G. (2020). Identification of region-specific astrocyte subtypes at single cell resolution. *Nature Communications*, 11(1), 1220. <https://doi.org/10.1038/s41467-019-14198-8>
- Bayraktar, O. A., Bartels, T., Holmqvist, S., Kleshchevnikov, V., Martirosyan, A., Polioudakis, D., Ben Haim, L., Young, A. M. H., Batiuk, M. Y., Prakash, K., Brown, A., Roberts, K., Paredes, M. F., Kawaguchi, R., Stockley, J. H., Sabeur, K., Chang, S. M., Huang, E., Hutchinson, P., ... Rowitch, D. H. (2020). Astrocyte layers in the mammalian cerebral cortex revealed by a single-cell in situ transcriptomic map. *Nature Neuroscience*, 23(4), 500–509. <https://doi.org/10.1038/s41593-020-0602-1>
- Belousov, A. B., Fontes, J. D., Freitas-Andrade, M., & Naus, C. C. (2017). Gap junctions and hemichannels: Communicating cell death in neurodevelopment and disease. *BMC Cell Biology*, 18(1), 4. <https://doi.org/10.1186/s12860-016-0120-x>
- Benarroch, E. E. (2005). Neuron-astrocyte interactions: Partnership for normal function and disease in the central nervous system. *Mayo Clinic Proceedings*, 80(10), 1326–1338. <https://doi.org/10.4065/80.10.1326>
- Bolton, S., Greenwood, K., Hamilton, N., & Butt, A. M. (2006). Regulation of the astrocyte resting membrane potential by cyclic AMP and protein kinase A. *Glia*, 54(4), 316–328. <https://doi.org/10.1002/glia.20384>
- Bordoni, L., Thoren, A. E., Gutiérrez-Jiménez, E., Åbjørnsbråten, K. S., Bjørnstad, D. M., Tang, W., Stern, M., Østergaard, L., Nagelhus, E. A., Frische, S., Ottersen, O. P., & Enger, R. (2023). Deletion of aquaporin-4 improves capillary blood flow distribution in brain edema. *Glia*, 71(11), 2559–2572. <https://doi.org/10.1002/glia.24439>
- Boulay, A.-C., Gilbert, A., Oliveira Moreira, V., Blugeon, C., Perrin, S., Pouch, J., Le Crom, S., Ducos, B., & Cohen-Salmon, M. (2018). Connexin 43 controls the astrocyte immunoregulatory phenotype. *Brain Sciences*, 8(4), 50. <https://doi.org/10.3390/brainsci8040050>
- Boulay, A.-C., Mazeraud, A., Cisternino, S., Saubaméa, B., Mailly, P., Jourden, L., Blugeon, C., Mignon, V., Smirnova, M., Cavallo, A., Ezan, P., Avé, P., Dingli, F., Loew, D., Vieira, P., Chrétien, F., & Cohen-Salmon, M. (2015). Immune quiescence of the brain is set by astroglial connexin 43. *The Journal of Neuroscience*, 35(10), 4427–4439. <https://doi.org/10.1523/JNEUROSCI.2575-14.2015>
- Boulay, A.-C., Saubaméa, B., Cisternino, S., Mignon, V., Mazeraud, A., Jourden, L., Blugeon, C., & Cohen-Salmon, M. (2015). The Sarcoglycan complex is expressed in the cerebrovascular system and is specifically regulated by astroglial Cx30 channels. *Frontiers in Cellular Neuroscience*, 9, 9. <https://doi.org/10.3389/fncel.2015.00009>
- Bruzzone, R., White, T. W., & Paul, D. L. (1996). Connections with connexins: The molecular basis of direct intercellular signaling. *European Journal of Biochemistry*, 238(1), 1–27. <https://doi.org/10.1111/j.1432-1033.1996.0001q.x>
- Cibelli, A., Stout, R., Timmermann, A., De Menezes, L., Guo, P., Maass, K., Seifert, G., Steinhäuser, C., Spray, D. C., & Scemes, E. (2021). Cx43 carboxyl terminal domain determines AQP4 and Cx30 endfoot organization and blood brain barrier permeability. *Scientific Reports*, 11(1), 24334. <https://doi.org/10.1038/s41598-021-03694-x>
- Clément, T., Rodriguez-Grande, B., & Badaut, J. (2020). Aquaporins in brain edema. *Journal of Neuroscience Research*, 98(1), 9–18. <https://doi.org/10.1002/jnr.24354>
- Dalléac, G., Chever, O., & Rouach, N. (2013). How do astrocytes shape synaptic transmission? Insights from electrophysiology. *Frontiers in Cellular Neuroscience*, 7, 159. <https://doi.org/10.3389/fncel.2013.00159>
- De Bock, M., Leybaert, L., & Giaume, C. (2017). Connexin channels at the glio-vascular interface: Gatekeepers of the brain. *Neurochemical Research*, 42(9), 2519–2536. <https://doi.org/10.1007/s11064-017-2313-x>
- De Bock, M., Vandenbroucke, R. E., Decrock, E., Culot, M., Cecchelli, R., & Leybaert, L. (2014). A new angle on blood-CNS interfaces: A role for connexins? *FEBS Letters*, 588(8), 1259–1270. <https://doi.org/10.1016/j.febslet.2014.02.060>
- Díaz-Castro, B., Robel, S., & Mishra, A. (2023). Astrocyte endfeet in brain function and pathology: Open questions. *Annual Review of Neuroscience*, 46(1), 101–121. <https://doi.org/10.1146/annurev-neuro-091922-031205>
- Dodge, Y. (2008). *The concise encyclopedia of statistics* (1st ed.). Springer.
- Du, Y., Ma, B., Kiyoshi, C. M., Alford, C. C., Wang, W., & Zhou, M. (2015). Freshly dissociated mature hippocampal astrocytes exhibit passive membrane conductance and low membrane resistance similarly to synaptic coupled astrocytes. *Journal of Neurophysiology*, 113(10), 3744–3750. <https://doi.org/10.1152/jn.00206.2015>

- Dunn, K. M., Hill-Eubanks, D. C., Liedtke, W. B., & Nelson, M. T. (2013). TRPV4 channels stimulate Ca²⁺-induced Ca²⁺ release in astrocytic endfeet and amplify neurovascular coupling responses. *Proceedings of the National Academy of Sciences*, 110(15), 6157–6162. <https://doi.org/10.1073/pnas.1216514110>
- Eilert-Olsen, M., Haj-Yasein, N. N., Vindedal, G. F., Enger, R., Gundersen, G. A., Hoddevik, E. H., Petersen, P. H., Haug, F.-M. S., Skare, Ø., Adams, M. E., Froehner, S. C., Burkhardt, J. M., Thoren, A. E., & Nagelhus, E. A. (2012). Deletion of aquaporin-4 changes the perivascular glial protein scaffold without disrupting the brain endothelial barrier. *Glia*, 60(3), 432–440. <https://doi.org/10.1002/glia.22277>
- El-Khoury, N., Braun, A., Hu, F., Pandey, M., Nedergaard, M., Lagamma, E. F., & Ballabh, P. (2006). Astrocyte end-feet in germinal matrix, cerebral cortex, and white matter in developing infants. *Pediatric Research*, 59(5), 673–679. <https://doi.org/10.1203/01.pdr.0000214975.85311.9c>
- Endo, F., Kasai, A., Soto, J. S., Yu, X., Qu, Z., Hashimoto, H., Gradinaru, V., Kawaguchi, R., & Khakh, B. S. (2022). Molecular basis of astrocyte diversity and morphology across the CNS in health and disease. *Science*, 378(6619), eadc9020. <https://doi.org/10.1126/science.adc9020>
- Eroglu, C., & Barres, B. A. (2010). Regulation of synaptic connectivity by glia. *Nature*, 468(7321), 223–231. <https://doi.org/10.1038/nature09612>
- Errede, M., Benagiano, V., Girolamo, F., Flace, P., Bertossi, M., Roncali, L., & Virgintino, D. (2002). Differential expression of connexin43 in foetal, adult and tumour-associated human brain endothelial cells. *The Histochemical Journal*, 34(6–7), 265–271. <https://doi.org/10.1023/a:1023344106815>
- Ezan, P., André, P., Cisternino, S., Saubaméa, B., Boulay, A.-C., Doutremer, S., Thomas, M.-A., Quenec'h du, N., Giaume, C., & Cohen-Salmon, M. (2012). Deletion of astroglial connexins weakens the blood–brain barrier. *Journal of Cerebral Blood Flow & Metabolism*, 32(8), 1457–1467. <https://doi.org/10.1038/jcbfm.2012.45>
- Fukuda, A. M., Adami, A., Pop, V., Bellone, J. A., Coats, J. S., Hartman, R. E., Ashwal, S., Obenaus, A., & Badaut, J. (2013). Posttraumatic reduction of edema with aquaporin-4 RNA interference improves acute and chronic functional recovery. *Journal of Cerebral Blood Flow and Metabolism: Official Journal of the International Society of Cerebral Blood Flow and Metabolism*, 33(10), 1621–1632. <https://doi.org/10.1038/jcbfm.2013.118>
- Galea, I. (2021). The blood–brain barrier in systemic infection and inflammation. *Cellular & Molecular Immunology*, 18(11), 2489–2501. <https://doi.org/10.1038/s41423-021-00757-x>
- Ganat, Y. M., Silbereis, J., Cave, C., Ngu, H., Anderson, G. M., Ohkubo, Y., Ment, L. R., & Vaccarino, F. M. (2006). Early postnatal astroglial cells produce multilineage precursors and neural stem cells in vivo. *The Journal of Neuroscience*, 26(33), 8609–8621. <https://doi.org/10.1523/JNEUROSCI.2532-06.2006>
- Genet, N., Genet, G., Chavkin, N. W., Paila, U., Fang, J. S., Vasavada, H. H., Goldberg, J. S., Acharya, B. R., Bhatt, N. S., Baker, K., McDonnell, S. P., Huba, M., Sankaranarayanan, D., Ma, G. Z. M., Eichmann, A., Thomas, J.-L., French-Constant, C., & Hirschi, K. K. (2023). Connexin 43-mediated neurovascular interactions regulate neurogenesis in the adult brain subventricular zone. *Cell Reports*, 42(4), 112371. <https://doi.org/10.1016/j.celrep.2023.112371>
- Giaume, C., Koulikoff, A., Roux, L., Holcman, D., & Rouach, N. (2010). Astroglial networks: A step further in neuroglial and gliovascular interactions. *Nature Reviews Neuroscience*, 11(2), 87–99. <https://doi.org/10.1038/nrn2757>
- Giaume, C., Leybaert, L., Naus, C., & Sáez, J.-C. (2013). Connexin and pannexin hemichannels in brain glial cells: Properties, pharmacology, and roles. *Frontiers in Pharmacology*, 4, 88. <https://doi.org/10.3389/fphar.2013.00088>
- González, J., Pinzón, A., Angarita-Rodríguez, A., Aristizabal, A. F., Barreto, G. E., & Martín-Jiménez, C. (2020). Advances in astrocyte computational models: From metabolic reconstructions to multi-omic approaches. *Frontiers in Neuroinformatics*, 14, 35. <https://doi.org/10.3389/fninf.2020.00035>
- Haj-Yasein, N. N., Jensen, V., Østby, I., Omholt, S. W., Voipio, J., Kaila, K., Ottersen, O. P., Hvalby, Ø., & Nagelhus, E. A. (2012). Aquaporin-4 regulates extracellular space volume dynamics during high-frequency synaptic stimulation: A gene deletion study in mouse hippocampus. *Glia*, 60(6), 867–874. <https://doi.org/10.1002/glia.22319>
- Haj-Yasein, N. N., Vindedal, G. F., Eilert-Olsen, M., Gundersen, G. A., Skare, Ø., Laake, P., Klungland, A., Thorén, A. E., Burkhardt, J. M., Ottersen, O. P., & Nagelhus, E. A. (2011). Glial-conditional deletion of aquaporin-4 (Aqp4) reduces blood–brain water uptake and confers barrier function on perivascular astrocyte endfeet. *Proceedings of the National Academy of Sciences*, 108(43), 17815–17820. <https://doi.org/10.1073/pnas.1110655108>
- Heller, J. P., & Rusakov, D. A. (2019). A method to visualize the nanoscopic morphology of astrocytes in vitro and in situ. In B. di Benedetto (Ed.), *Astrocytes: Methods and protocols* (pp. 69–84). Springer. https://doi.org/10.1007/978-1-4939-9068-9_5
- Holt, M. G. (2023). Astrocyte heterogeneity and interactions with local neural circuits. *Essays in Biochemistry*, 67(1), 93–106. <https://doi.org/10.1042/EBC20220136>
- Hornig, S., Therattil, A., Moyon, S., Gordon, A., Kim, K., Argaw, A. T., Hara, Y., Mariani, J. N., Sawai, S., Flodby, P., Crandall, E. D., Borok, Z., Sofroniew, M. V., Chapouly, C., & John, G. R. (2017). Astrocytic tight junctions control inflammatory CNS lesion pathogenesis. *Journal of Clinical Investigation*, 127(8), 3136–3151. <https://doi.org/10.1172/JCI91301>
- Höslj, L., Binini, N., Ferrari, K. D., Thieren, L., Looser, Z. J., Zuend, M., Zanker, H. S., Berry, S., Holub, M., Möbius, W., Ruhwedel, T., Nave, K.-A., Giaume, C., Weber, B., & Saab, A. S. (2022). Decoupling astrocytes in adult mice impairs synaptic plasticity and spatial learning. *Cell Reports*, 38(10), 110484. <https://doi.org/10.1016/j.celrep.2022.110484>
- Höslj, L., Zuend, M., Bredell, G., Zanker, H. S., Porto de Oliveira, C. E., Saab, A. S., & Weber, B. (2022). Direct vascular contact is a hallmark of cerebral astrocytes. *Cell Reports*, 39(1), 110599. <https://doi.org/10.1016/j.celrep.2022.110599>
- Huang, X., Su, Y., Wang, N., Li, H., Li, Z., Yin, G., Chen, H., Niu, J., & Yi, C. (2021). Astroglial connexins in neurodegenerative diseases. *Frontiers in Molecular Neuroscience*, 14, 657514. <https://doi.org/10.3389/fnmol.2021.657514>
- Idziak, A., Inavalli, V. V. G. K., Bancelin, S., Arizono, M., & Nägerl, U. V. (2023). The impact of chemical fixation on the microanatomy of mouse brain tissue. *Neuroscience*, 10, 0104-23. <https://doi.org/10.1101/2023.02.21.528828>
- John Lin, C.-C., Yu, K., Hatcher, A., Huang, T.-W., Lee, H. K., Carlson, J., Weston, M. C., Chen, F., Zhang, Y., Zhu, W., Mohila, C. A., Ahmed, N., Patel, A. J., Arenkiel, B. R., Noebels, J. L., Creighton, C. J., & Deneen, B. (2017). Identification of diverse astrocyte populations and their malignant analogs. *Nature Neuroscience*, 20(3), 396–405. <https://doi.org/10.1038/nn.4493>
- Jurga, A. M., Paleczna, M., Kadluczka, J., & Kuter, K. Z. (2021). Beyond the GFAP-astrocyte protein markers in the brain. *Biomolecules*, 11(9), 1361. <https://doi.org/10.3390/biom11091361>
- Kalisvaart, A. C. J., Abraham, A. H., Coney, A. T., Gu, S., & Colbourne, F. (2023). Intracranial pressure dysfunction following severe intracerebral hemorrhage in middle-aged rats. *Translational Stroke Research*, 14(6), 970–986. <https://doi.org/10.1007/s12975-022-01102-8>
- Katoozi, S., Skauli, N., Rahmani, S., Camassa, L. M. A., Boldt, H. B., Ottersen, O. P., & Amiry-Moghaddam, M. (2017). Targeted deletion of Aqp4 promotes the formation of astrocytic gap junctions. *Brain*

- Structure & Function*, 22(9), 3959–3972. <https://doi.org/10.1007/s00429-017-1448-5>
- Keller, D., Erö, C., & Markram, H. (2018). Cell densities in the mouse brain: A systematic review. *Frontiers in Neuroanatomy*, 12, 83. <https://doi.org/10.3389/fnana.2018.00083>
- Khakh, B. S., & Sofroniew, M. V. (2015). Diversity of astrocyte functions and phenotypes in neural circuits. *Nature Neuroscience*, 18(7), 942–952. <https://doi.org/10.1038/nn.4043>
- Kim, H., Kim, M., Im, S.-K., & Fang, S. (2018). Mouse Cre-LoxP system: General principles to determine tissue-specific roles of target genes. *Laboratory Animal Research*, 34(4), 147–159. <https://doi.org/10.5625/lar.2018.34.4.147>
- Kim, Y., Park, J., & Choi, Y. K. (2019). The role of astrocytes in the central nervous system focused on BK channel and heme oxygenase metabolites: A review. *Antioxidants*, 8(5), 121. <https://doi.org/10.3390/antiox8050121>
- Kiyoshi, C. M., & Zhou, M. (2019). Astrocyte syncytium: A functional reticular system in the brain. *Neural Regeneration Research*, 14(4), 595–596. <https://doi.org/10.4103/1673-5374.247462>
- Korogod, N., Petersen, C. C., & Knott, G. W. (2015). Ultrastructural analysis of adult mouse neocortex comparing aldehyde perfusion with cryo fixation. *eLife*, 4, e05793. <https://doi.org/10.7554/eLife.05793>
- Kubotera, H., Ikeshima-Kataoka, H., Hatashita, Y., Allegra Mascaro, A. L., Pavone, F. S., & Inoue, T. (2019). Astrocytic endfeet re-cover blood vessels after removal by laser ablation. *Scientific Reports*, 9(1), 1263. <https://doi.org/10.1038/s41598-018-37419-4>
- Langer, J., Gerkau, N. J., Derouiche, A., Kleinhans, C., Moshrefi-Ravasdjani, B., Fredrich, M., Kafitz, K. W., Seifert, G., Steinhäuser, C., & Rose, C. R. (2017). Rapid sodium signaling couples glutamate uptake to breakdown of ATP in perivascular astrocyte endfeet. *Glia*, 65(2), 293–308. <https://doi.org/10.1002/glia.23092>
- Lanjakornsiripan, D., Pior, B.-J., Kawaguchi, D., Furutachi, S., Tahara, T., Katsuyama, Y., Suzuki, Y., Fukazawa, Y., & Gotoh, Y. (2018). Layer-specific morphological and molecular differences in neocortical astrocytes and their dependence on neuronal layers. *Nature Communications*, 9(1), 1623. <https://doi.org/10.1038/s41467-018-03940-3>
- Lawal, O., Ulloa Severino, F. P., & Eroglu, C. (2022). The role of astrocyte structural plasticity in regulating neural circuit function and behavior. *Glia*, 70(8), 1467–1483. <https://doi.org/10.1002/glia.24191>
- Legland, D., Arganda-Carreras, I., & Andrey, P. (2016). MorphoLibJ: Integrated library and plugins for mathematical morphology with ImageJ. *Bioinformatics*, 32(22), 3532–3534. <https://doi.org/10.1093/bioinformatics/btw413>
- Liang, Z., Wang, X., Hao, Y., Qiu, L., Lou, Y., Zhang, Y., Ma, D., & Feng, J. (2020). The multifaceted role of astrocyte connexin 43 in ischemic stroke through forming hemichannels and gap junctions. *Frontiers in Neurology*, 11, 703. <https://doi.org/10.3389/fneur.2020.00703>
- Lorin, C., Gueffier, M., Bois, P., Faivre, J.-F., Cognard, C., & Sebille, S. (2013). Ultrastructural and functional alterations of EC coupling elements in mdx cardiomyocytes: An analysis from membrane surface to depth. *Cell Biochemistry and Biophysics*, 66(3), 723–736. <https://doi.org/10.1007/s12013-013-9517-8>
- Ma, B., Xu, G., Wang, W., Enyart, J. J., & Zhou, M. (2014). Dual patch voltage clamp study of low membrane resistance astrocytes in situ. *Molecular Brain*, 7(1), 18. <https://doi.org/10.1186/1756-6606-7-18>
- Ma, T., Yang, B., Gillespie, A., Carlson, E. J., Epstein, C. J., & Verkman, A. S. (1997). Generation and phenotype of a transgenic knockout mouse lacking the mercurial-insensitive water channel aquaporin-4. *The Journal of Clinical Investigation*, 100(5), 957–962. <https://doi.org/10.1172/JCI231>
- MacAulay, N. (2021). Molecular mechanisms of brain water transport. *Nature Reviews Neuroscience*, 22(6), 326–344. <https://doi.org/10.1038/s41583-021-00454-8>
- Madisen, L., Zwingman, T. A., Sunkin, S. M., Oh, S. W., Zariwala, H. A., Gu, H., Ng, L. L., Palmiter, R. D., Hawrylycz, M. J., Jones, A. R., Lein, E. S., & Zeng, H. (2010). A robust and high-throughput Cre reporting and characterization system for the whole mouse brain. *Nature Neuroscience*, 13(1), 133–140. <https://doi.org/10.1038/nn.2467>
- Markram, H., Muller, E., Ramaswamy, S., Reimann, M. W., Abdellah, M., Sanchez, C. A., Ailamaki, A., Alonso-Nanclares, L., Antille, N., Arsever, S., Kahou, G. A. A., Berger, T. K., Bilgili, A., Buncic, N., Chalimourda, A., Chindemi, G., Courcol, J.-D., Delalandre, F., Delattre, V., ... Schürmann, F. (2015). Reconstruction and simulation of neocortical microcircuitry. *Cell*, 163(2), 456–492. <https://doi.org/10.1016/j.cell.2015.09.029>
- Matejuk, A., & Ransohoff, R. M. (2020). Crosstalk between astrocytes and microglia: An overview. *Frontiers in Immunology*, 11, 1416. <https://doi.org/10.3389/fimmu.2020.01416>
- Mathiisen, T. M., Lehre, K. P., Danbolt, N. C., & Ottersen, O. P. (2010). The perivascular astroglial sheath provides a complete covering of the brain microvessels: An electron microscopic 3D reconstruction. *Glia*, 58(9), 1094–1103. <https://doi.org/10.1002/glia.20990>
- Mattei, B., Lira, R. B., Perez, K. R., & Riske, K. A. (2017). Membrane permeabilization induced by triton X-100: The role of membrane phase state and edge tension. *Chemistry and Physics of Lipids*, 202, 28–37. <https://doi.org/10.1016/j.chemphyslip.2016.11.009>
- McNeill, J., Rudyk, C., Hildebrand, M. E., & Salmaso, N. (2021). Ion channels and electrophysiological properties of astrocytes: Implications for emergent stimulation technologies. *Frontiers in Cellular Neuroscience*, 15, 183. <https://doi.org/10.3389/fncel.2021.644126>
- Molina-Gonzalez, I., Holloway, R. K., Jiwaji, Z., Dando, O., Kent, S. A., Emelianova, K., Lloyd, A. F., Forbes, L. H., Mahmood, A., Skripuletz, T., Gudi, V., Febery, J. A., Johnson, J. A., Fowler, J. H., Kuhlmann, T., Williams, A., Chandran, S., Stangel, M., Howden, A. J. M., ... Miron, V. E. (2023). Astrocyte-oligodendrocyte interaction regulates central nervous system regeneration. *Nature Communications*, 14(1), 3372. <https://doi.org/10.1038/s41467-023-39046-8>
- Moye, S. L., Diaz-Castro, B., Gangwani, M. R., & Khakh, B. S. (2019). Visualizing astrocyte morphology using Lucifer yellow iontophoresis. *Journal of Visualized Experiments: JoVE*, 151, e60225. <https://doi.org/10.3791/60225>
- Nagy, J. I., Dudek, F. E., & Rash, J. E. (2004). Update on connexins and gap junctions in neurons and glia in the mammalian nervous system. *Brain Research Reviews*, 47(1), 191–215. <https://doi.org/10.1016/j.brainresrev.2004.05.005>
- Nakase, T., & Naus, C. C. G. (2004). Gap junctions and neurological disorders of the central nervous system. *Biochimica et Biophysica Acta (BBA)-Biomembranes*, 1662(1), 149–158. <https://doi.org/10.1016/j.bbamem.2004.01.009>
- Neely, J. D., Amiry-Moghaddam, M., Ottersen, O. P., Froehner, S. C., Agre, P., & Adams, M. E. (2001). Syntrophin-dependent expression and localization of aquaporin-4 water channel protein. *Proceedings of the National Academy of Sciences of the United States of America*, 98(24), 14108–14113. <https://doi.org/10.1073/pnas.241508198>
- Nielsen, S., Arnulf Nagelhus, E., Amiry-Moghaddam, M., Bourque, C., Agre, P., & Pette Ottersen, O. (1997). Specialized membrane domains for water transport in glial cells: High-resolution immunogold cytochemistry of aquaporin-4 in rat brain. *The Journal of Neuroscience*, 17(1), 171–180. <https://doi.org/10.1523/JNEUROSCI.17-01-00171.1997>
- Nolte, C., Matyash, M., Pivneva, T., Schipke, C. G., Ohlemeyer, C., Hanisch, U.-K., Kirchhoff, F., & Kettenmann, H. (2001). GFAP promoter-controlled EGFP-expressing transgenic mice: A tool to visualize astrocytes and astrogliosis in living brain tissue. *Glia*, 33(1), 72–86. [https://doi.org/10.1002/1098-1136\(20010101\)33:1<72::AID-GLIA1007>3.0.CO;2-A](https://doi.org/10.1002/1098-1136(20010101)33:1<72::AID-GLIA1007>3.0.CO;2-A)



- Obermeier, B., Daneman, R., & Ransohoff, R. M. (2013). Development, maintenance and disruption of the blood-brain barrier. *Nature Medicine*, 19(12), 1584–1596. <https://doi.org/10.1038/nm.3407>
- Ollion, J., Cochennec, J., Loll, F., Escudé, C., & Boudier, T. (2013). TANGO: A generic tool for high-throughput 3D image analysis for studying nuclear organization. *Bioinformatics*, 29(14), 1840–1841. <https://doi.org/10.1093/bioinformatics/btt276>
- Olude, M. A., Mustapha, O. A., Aderounmu, O. A., Olopade, J. O., & Ihunwo, A. O. (2015). Astrocyte morphology, heterogeneity, and density in the developing African giant rat (*Cricetomys gambianus*). *Frontiers in Neuroanatomy*, 9, 67. <https://doi.org/10.3389/fnana.2015.00067>
- Owens, T., Bechmann, I., & Engelhardt, B. (2008). Perivascular spaces and the two steps to neuroinflammation. *Journal of Neuropathology & Experimental Neurology*, 67(12), 1113–1121. <https://doi.org/10.1097/NEN.0b013e31818f9ca8>
- Palazzo, C., Buccoliero, C., Mola, M. G., Abbrescia, P., Nicchia, G. P., Trojano, M., & Frigeri, A. (2019). AQP4ex is crucial for the anchoring of AQP4 at the astrocyte end-feet and for neuromyelitis optica antibody binding. *Acta Neuropathologica Communications*, 7(1), 51. <https://doi.org/10.1186/s40478-019-0707-5>
- Panchenko, P. E., Hippauf, L., Konsman, J. P., & Badaut, J. (2023). Do astrocytes act as immune cells after pediatric TBI? *Neurobiology of Disease*, 185, 106231. <https://doi.org/10.1016/j.nbd.2023.106231>
- Pandit, R., Chen, L., & Götz, J. (2020). The blood-brain barrier: Physiology and strategies for drug delivery. *Advanced Drug Delivery Reviews*, 165–166, 1–14. <https://doi.org/10.1016/j.addr.2019.11.009>
- Park, Y. M., Chun, H., Shin, J.-I., & Lee, C. J. (2018). Astrocyte specificity and coverage of hGFAP-CreERT2 [Tg(GFAP-Cre/ERT2)13Kdmc] mouse line in various brain regions. *Experimental Neurobiology*, 27(6), 508–525. <https://doi.org/10.5607/en.2018.27.6.508>
- Pathak, D., & Sriram, K. (2023). Neuron-astrocyte omnidirectional signaling in neurological health and disease. *Frontiers in Molecular Neuroscience*, 16, 1169320. <https://doi.org/10.3389/fnmol.2023.1169320>
- Pedreñez, A., Mosquera-Sulbarán, J., Muñoz, N., Tene, D., & Robalino, J. (2021). Nanoantibodies: Small molecules, big possibilities. *Biotechnology*, 102(3), 321–336. <https://doi.org/10.5114/bta.2021.108724>
- Planche, V., Manjon, J. V., Mansencal, B., Lanuza, E., Tourdias, T., Catheline, G., & Coupé, P. (2022). Structural progression of Alzheimer's disease over decades: The MRI staging scheme. *Brain Communications*, 4(3), fcac109. <https://doi.org/10.1093/braincomms/fcac109>
- Ponti, A., Schwarb, P., Gulati, A., & Baker, V. (2007). Huygens remote manager: A web interface for high-volume batch deconvolution. *Imaging & Microscopy*, 9(2), 57–58.
- Preston, A. N., Cervasio, D. A., & Laughlin, S. T. (2019). Visualizing the brain's astrocytes. *Methods in Enzymology*, 622, 129–151. <https://doi.org/10.1016/bs.mie.2019.02.006>
- Quintana, F. J. (2017). Astrocytes to the rescue! Glia limitans astrocytic endfeet control CNS inflammation. *The Journal of Clinical Investigation*, 127(8), 2897–2899. <https://doi.org/10.1172/JCI95769>
- Refaeli, R., Doron, A., Benmelech-Chovav, A., Groyzman, M., Kreisel, T., Loewenstein, Y., & Goshen, I. (2021). Features of hippocampal astrocytic domains and their spatial relation to excitatory and inhibitory neurons. *Glia*, 69(10), 2378–2390. <https://doi.org/10.1002/glia.24044>
- Rodríguez, J. J., Terzieva, S., Olabarria, M., Lanza, R. G., & Verkhratsky, A. (2013). Enriched environment and physical activity reverse astroglial degeneration in the hippocampus of AD transgenic mice. *Cell Death & Disease*, 4(6), e678. <https://doi.org/10.1038/cddis.2013.194>
- Rouach, N., Koulakoff, A., Abudara, V., Willecke, K., & Giaume, C. (2008). Astroglial metabolic networks sustain hippocampal synaptic transmission. *Science*, 322(5907), 1551–1555. <https://doi.org/10.1126/science.1164022>
- Saadoun, S., Tait, M. J., Reza, A., Davies, D. C., Bell, B. A., Verkman, A. S., & Papadopoulos, M. C. (2009). AQP4 gene deletion in mice does not alter blood-brain barrier integrity or brain morphology. *Neuroscience*, 161(3), 764–772. <https://doi.org/10.1016/j.neuroscience.2009.03.069>
- Saint-Martin, M., & Goda, Y. (2023). Astrocyte-synapse interactions and cell adhesion molecules. *The FEBS Journal*, 290(14), 3512–3526. <https://doi.org/10.1111/febs.16540>
- Sakr, N., Glazova, O., Shevkova, L., Onyanov, N., Kaziakhmedova, S., Shilova, A., Vorontsova, M. V., & Volchkov, P. (2023). Characterizing and quenching autofluorescence in fixed mouse adrenal cortex tissue. *International Journal of Molecular Sciences*, 24(4), 3432. <https://doi.org/10.3390/ijms24043432>
- Salman, M. M., Kitchen, P., Halsey, A., Wang, M. X., Törnroth-Horsefield, S., Conner, A. C., Badaut, J., Iliff, J. J., & Bill, R. M. (2022). Emerging roles for dynamic aquaporin-4 subcellular relocalization in CNS water homeostasis. *Brain*, 145(1), 64–75. <https://doi.org/10.1093/brain/awab311>
- Salmon, C. K., Syed, T. A., Kacerovsky, J. B., Alivodej, N., Schober, A. L., Sloan, T. F. W., Pratte, M. T., Rosen, M. P., Green, M., Chirgwin-Dasgupta, A., Mehta, S., Jilani, A., Wang, Y., Vali, H., Mandato, C. A., Siddiqi, K., & Murai, K. K. (2023). Organizing principles of astrocytic nanoarchitecture in the mouse cerebral cortex. *Current Biology*, 33(5), 957–972.e5. <https://doi.org/10.1016/j.cub.2023.01.043>
- Sánchez, O. F., Rodríguez, A. V., Velasco-España, J. M., Murillo, L. C., Sutachan, J.-J., & Albarracín, S.-L. (2020). Role of connexins 30, 36, and 43 in brain tumors, neurodegenerative diseases, and neuroprotection. *Cells*, 9(4), 846. <https://doi.org/10.3390/cells9040846>
- Schindelin, J., Arganda-Carreras, I., Frise, E., Kaynig, V., Longair, M., Pietzsch, T., Preibisch, S., Rueden, C., Saalfeld, S., Schmid, B., Tinevez, J.-Y., White, D. J., Hartenstein, V., Eliceiri, K., Tomancak, P., & Cardona, A. (2012). Fiji: An open-source platform for biological-image analysis. *Nature Methods*, 9(7), 676–682. <https://doi.org/10.1038/nmeth.2019>
- Schreiner, B., Romanelli, E., Liberski, P., Ingold-Heppner, B., Sobottka-Brillout, B., Hartwig, T., Chandrasekar, V., Johannsen, H., Zeilhofer, H. U., Aguzzi, A., Heppner, F., Kerschensteiner, M., & Becher, B. (2015). Astrocyte depletion impairs redox homeostasis and triggers neuronal loss in the adult CNS. *Cell Reports*, 12(9), 1377–1384. <https://doi.org/10.1016/j.celrep.2015.07.051>
- Simard, M., Arcuino, G., Takano, T., Liu, Q. S., & Nedergaard, M. (2003). Signaling at the gliovascular interface. *Journal of Neuroscience*, 23(27), 9254–9262. <https://doi.org/10.1523/JNEUROSCI.23-27-09254.2003>
- Smith, A. J., & Verkman, A. S. (2015). Super resolution imaging of aquaporin-4 cluster size in antibody-stained paraffin brain sections. *Biophysical Journal*, 109(12), 2511–2522. <https://doi.org/10.1016/j.bpj.2015.10.047>
- Söhl, G., Odermatt, B., Maxeiner, S., Degen, J., & Willecke, K. (2004). New insights into the expression and function of neural connexins with transgenic mouse mutants. *Brain Research Reviews*, 47(1), 245–259. <https://doi.org/10.1016/j.brainresrev.2004.05.006>
- Spearman, C. (1904). The proof and measurement of association between two things. *The American Journal of Psychology*, 15(1), 72. <https://doi.org/10.2307/1412159>
- Srinivasan, R., Lu, T.-Y., Chai, H., Xu, J., Huang, B. S., Golshani, P., Coppola, G., & Khakh, B. S. (2016). New transgenic mouse lines for selectively targeting astrocytes and studying calcium signals in astrocyte processes in situ and in vivo. *Neuron*, 92(6), 1181–1195. <https://doi.org/10.1016/j.neuron.2016.11.030>
- Stokum, J. A., Shim, B., Huang, W., Kane, M., Smith, J. A., Gerzanich, V., & Simard, J. M. (2021). A large portion of the astrocyte proteome is dedicated to perivascular endfeet, including critical components of the electron transport chain. *Journal of Cerebral Blood Flow & Metabolism*, 41(10), 2546–2560. <https://doi.org/10.1177/0271678X211004182>
- Stout, R. F., Snapp, E. L., & Spray, D. C. (2015). Connexin type and fluorescent protein fusion tag determine structural stability of gap junction

- plaques. *Journal of Biological Chemistry*, 290(39), 23497–23514. <https://doi.org/10.1074/jbc.M115.659979>
- Tait, M. J., Saadoun, S., Bell, B. A., & Papadopoulos, M. C. (2008). Water movements in the brain: Role of aquaporins. *Trends in Neurosciences*, 31(1), 37–43. <https://doi.org/10.1016/j.tins.2007.11.003>
- Tang, T., Yuan, L., Wang, K., & Zhao, M. (2021). *Unfavorable Effects of Fixatives on the Fluorescence Intensity and Biological Functions of Fluorescent Proteins in HEK293T Cells and Transgenic Mice*. In Review. <https://doi.org/10.21203/rs.3.rs-764380/v1>
- Theofilas, P., Steinhäuser, C., Theis, M., & Derouiche, A. (2017). Morphological study of a connexin 43-GFP reporter mouse highlights glial heterogeneity, amacrine cells, and olfactory ensheathing cells. *Journal of Neuroscience Research*, 95(11), 2182–2194. <https://doi.org/10.1002/jnr.24055>
- Van Campenhout, R., Gomes, A. R., De Groof, T. W. M., Muyldermans, S., Devoogdt, N., & Vinken, M. (2021). Mechanisms underlying connexin hemichannel activation in disease. *International Journal of Molecular Sciences*, 22(7), 3503. <https://doi.org/10.3390/ijms22073503>
- Vasile, F., Dossi, E., & Rouach, N. (2017). Human astrocytes: Structure and functions in the healthy brain. *Brain Structure and Function*, 222(5), 2017–2029. <https://doi.org/10.1007/s00429-017-1383-5>
- Venkat, P., Chopp, M., & Chen, J. (2017). CBF–metabolism coupling. In *Primer on cerebrovascular diseases* (pp. 67–70). Elsevier. <https://doi.org/10.1016/B978-0-12-803058-5.00012-6>
- Verkhatsky, A., & Nedergaard, M. (2018). Physiology of astroglia. *Physiological Reviews*, 98, 151.
- Viana, J. F., Machado, J. L., Abreu, D. S., Veiga, A., Barsanti, S., Tavares, G., Martins, M., Sardinha, V. M., Guerra-Gomes, S., Domingos, C., Pauletti, A., Wahis, J., Liu, C., Cali, C., Henneberger, C., Holt, M. G., & Oliveira, J. F. (2023). Astrocyte structural heterogeneity in the mouse hippocampus. *Glia*, 71(7), 1667–1682. <https://doi.org/10.1002/glia.24362>
- Vitale, A., & Ricceri, L. (2022). The principle of the 3Rs between aspiration and reality. *Frontiers in Physiology*, 13, 914939. <https://doi.org/10.3389/fphys.2022.914939>
- Wang, M. X., Ray, L., Tanaka, K. F., Iliff, J. J., & Heys, J. (2021). Varying perivascular astroglial endfoot dimensions along the vascular tree maintain perivascular-interstitial flux through the cortical mantle. *Glia*, 69(3), 715–728. <https://doi.org/10.1002/glia.23923>
- Wang, Y., Fu, A. K. Y., & Ip, N. Y. (2022). Instructive roles of astrocytes in hippocampal synaptic plasticity: Neuronal activity-dependent regulatory mechanisms. *The FEBS Journal*, 289(8), 2202–2218. <https://doi.org/10.1111/febs.15878>
- Weber, B., & Barros, L. F. (2015). The astrocyte: Powerhouse and recycling center. *Cold Spring Harbor Perspectives in Biology*, 7(12), a020396. <https://doi.org/10.1101/cshperspect.a020396>
- Welling, P. A. (2008). Scaffolding proteins in transport regulation. In *Seldin and Giebisch's the kidney* (pp. 325–341). Elsevier. <https://doi.org/10.1016/B978-012088488-9.50015-2>
- Yang, K., Liu, Y., & Zhang, M. (2024). The diverse roles of reactive astrocytes in the pathogenesis of amyotrophic lateral sclerosis. *Brain Sciences*, 14(2), 158. <https://doi.org/10.3390/brainsci14020158>
- Yau, C. N., Lai, H. M., Lee, K., Kwok, A. J., Huang, J., & Ko, H. (2023). Principles of deep immunohistochemistry for 3D histology. *Cell Reports Methods*, 3(5), 100458. <https://doi.org/10.1016/j.crmeth.2023.100458>
- Zhang, F., Peng, W., Sweeney, J. A., Jia, Z., & Gong, Q. (2018). Brain structure alterations in depression: Psychoradiological evidence. *CNS Neuroscience & Therapeutics*, 24(11), 994–1003. <https://doi.org/10.1111/cns.12835>
- Zhang, Y., Xu, K., Liu, Y., Erokwu, B. O., Zhao, P., Flask, C. A., Ramos-Estebanez, C., Farr, G. W., LaManna, J. C., Boron, W. F., & Yu, X. (2019). Increased cerebral vascularization and decreased water exchange across the blood–brain barrier in aquaporin-4 knockout mice. *PLoS One*, 14(6), e0218415. <https://doi.org/10.1371/journal.pone.0218415>
- Zhou, B., Zuo, Y.-X., & Jiang, R.-T. (2019). Astrocyte morphology: Diversity, plasticity, and role in neurological diseases. *CNS Neuroscience & Therapeutics*, 25(6), 665–673. <https://doi.org/10.1111/cns.13123>
- Zhou, C., Hu, X., Hu, J., Liang, M., Yin, X., Chen, L., Zhang, J., & Wang, J. (2016). Altered brain network in amyotrophic lateral sclerosis: A resting graph theory-based network study at voxel-wise level. *Frontiers in Neuroscience*, 10, 204. <https://doi.org/10.3389/fnins.2016.00204>
- Zhou, J., Kong, H., Hua, X., Xiao, M., Ding, J., & Hu, G. (2008). Altered blood–brain barrier integrity in adult aquaporin-4 knockout mice. *Neuroreport*, 19(1), 1–5. <https://doi.org/10.1097/WNR.0b013e3282f2b4eb>
- Zhou, M., Du, Y., Aten, S., & Terman, D. (2021). On the electrical passivity of astrocyte potassium conductance. *Journal of Neurophysiology*, 126(4), 1403–1419. <https://doi.org/10.1152/jn.00330.2021>
- Zhou, M., Schools, G. P., & Kimelberg, H. K. (2006). Development of GLAST(+) astrocytes and NG2(+) glia in rat hippocampus CA1: Mature astrocytes are electrophysiologically passive. *Journal of Neurophysiology*, 95(1), 134–143. <https://doi.org/10.1152/jn.00570.2005>
- Zisis, E., Keller, D., Kanari, L., Arnaudon, A., Gevaert, M., Delemontex, T., Coste, B., Foni, A., Abdellah, M., Cali, C., Hess, K., Magistretti, P. J., Schürmann, F., & Markram, H. (2021). Digital reconstruction of the neuro-glia-vascular architecture. *Cerebral Cortex*, 31(12), 5686–5703. <https://doi.org/10.1093/cercor/bhab254>
- Zwang, T. J., Bennett, R. E., Lysandrou, M., Woost, B., Zhang, A., Lieber, C. M., Richardson, D. S., & Hyman, B. T. (2023). Tissue libraries enable rapid determination of conditions that preserve antibody labeling in cleared mouse and human tissue. *eLife*, 12, e84112. <https://doi.org/10.7554/eLife.84112>

SUPPORTING INFORMATION

Additional supporting information can be found online in the Supporting Information section at the end of this article.

How to cite this article: Lorin, C., Guiet, R., Chiaruttini, N., Ambrosini, G., Boci, E., Abdellah, M., Markram, H., & Keller, D. (2024). Structural and molecular characterization of astrocyte and vasculature connectivity in the mouse hippocampus and cortex. *Glia*, 72(11), 2001–2021. <https://doi.org/10.1002/glia.24594>